

DESIGN OF THIN FILM SOLAR CELL MATERIAL STRUCTURE FOR RELIABILITY  
AND PERFORMANCE ROBUSTNESS

A Thesis by

Nita Yodo

Bachelor of Science, Wichita State University, 2011

Submitted to the Department of Industrial and Manufacturing Engineering  
and the faculty of the Graduate School of  
Wichita State University  
in partial fulfillment of  
the requirements for the degree of  
Master of Science

July, 2013

© Copyright 2013 by Nita Yodo

All Rights Reserved

DESIGN OF THIN FILM SOLAR CELL MATERIAL STRUCTURES FOR RELIABILITY  
AND PERFORMANCE ROBUSTNESS

The following faculty members have examined the final copy of this thesis for form and content, and recommend that it be accepted in partial fulfillment of the requirement for the degree of Master of Science, with a major in Industrial Engineering.

---

Pingfeng Wang, Committee Chair

---

Krishna Krishnan, Committee Member

---

Ramazan Asmatulu, Committee Member

## ACKNOWLEDGEMENTS

This thesis would not be complete without expressing my gratitude to several individuals who have helped and supported me in the preparation and completion of this study. While there are too many to individually thank, please remember that this work would not have been possible without your valuable assistance.

I owe my deepest gratitude to my advisor, Dr. Pingfeng Wang, who gave me trust and resources to conduct this research. His patient guidance, unfailing support, and understanding continually challenged me to excel. I would also like to extend my gratitude to Dr. Krishna Krishnan and Dr. Ramazan Asmatulu, for serving on my thesis committee.

To all my colleagues in the Reliability Engineering Automation Laboratory (REAL), I consider it a privilege to have worked with all of you. Thank you for your assistance, shared expertise, and also heartfelt friendship.

I greatly appreciate the many forms of support, encouragement, and unconditional love I have received from the amazing people around me: my parents, my brother, and my very best friend, Melvin Rafi.

Finally, this research would not have been possible without financial support from the National Science Foundation (NSF) under grant CMMI-1200597, and the Strategic Engineering Research Fellowship (SERF) by Wichita State University.

## ABSTRACT

Although a continued exponential growth of solar power generation over the world paves a path to a future in sustainable energy, development of photovoltaic (PV) technologies with low-cost and high-stability materials remains a challenge and has attracted tremendous attention to solar energy research. The prevalence of thin film solar cells substantially reduces the material costs. However, even in the presence of their band gap properties, a major issue faced by most thin film solar cells is the low output efficiency due to manufacturing variability and uncertain operating conditions. Thus, to ensure the reliability and performance robustness of thin film PV technologies, the design of the solar cell is studied.

To represent the thin film PV technologies, a copper gallium (di)selenide (CIGS) solar cell model is developed and optimized with the Reliability-based Robust Design Optimization (RBRDO) method. The main contribution of this research is the development of a probabilistic thin film solar cell model that considers the presence of the uncertainties in the PV system. This model takes into account the variability of the structure and the material properties of the CIGS solar cells, and assumes operation in ideal-weather conditions. A general reliability-based methodology to optimize the design of the CIGS PV technologies is presented in this research and this approach also could be used to facilitate the development and assessment of new PV technologies with more robust performance in efficiency and stability.

# TABLE OF CONTENTS

Chapter	Page
1. INTRODUCTION .....	1
1.1 Background and Motivation .....	1
1.1.1 Background of Solar Cell Technologies .....	2
1.1.2 Motivation.....	4
1.2 Research Objective and Scope.....	6
1.3 Thesis Overview .....	8
2. LITERATURE REVIEW .....	9
2.1 CIGS Characteristics.....	9
2.2 CIGS Solar Cell and Module Structure .....	11
2.2.1 ZnO:Al Front Contact .....	12
2.2.2 CdS Buffer Layer.....	13
2.2.3 CIGS Absorber Layer .....	14
2.2.4 Back Contact.....	15
2.2.5 Interconnect Structure.....	15
2.3 Modeling PV System .....	16
2.3.1 Cell Temperature .....	16
2.3.2 Light Generated Current .....	17
2.3.3 Diode Current.....	18
2.3.4 Resistance and Conductivity.....	19
2.3.5 Modeling PV Cells.....	21
2.3.6 Modeling PV Modules and PV Plants .....	24
3. MODELING APPROACH.....	27
3.1 Overview of Modeling Approach.....	27
3.2 Input Parameters .....	28
3.2.1 Operating Conditions.....	28
3.2.2 Manufacturer Specifications .....	29
3.3 Output Parameters.....	30
3.4 CIGS Modeling.....	31
3.4.1 Solar Cell Geometry Input.....	31
3.4.2 Model Implementation.....	32
3.5 Model Validation .....	36
3.6 Case study .....	38
3.6.1 Overview of the Case Studies .....	38
3.6.2 Results and Discussion .....	39

TABLE OF CONTENTS (continued)

Chapter	Page
4. DESIGN OPTIMIZATION OF SOLAR CELL MATERIAL STRUCTURE .....	43
4.1 Reliability-Based Robust Design Optimization (RBRDO) .....	43
4.2 Design Case Study .....	45
4.2.1 Description of the Design Problem .....	46
4.2.2 Design Case Study Results .....	47
5. CONCLUSIONS AND FUTURE WORK .....	51
5.1 Conclusions .....	51
5.2 Future Work .....	51
REFERENCES .....	52
APPENDICES .....	57
A. An Overview Ccomparison of Major PV Technologies (IRENA, 2012) .....	58
B. Process Flow of Monolithic Interconnection CIGS Module .....	59
C. Kirchoffs’s Law and Ohm’s Law .....	60
D. Experiment Set Up .....	61

## LIST OF TABLES

Tables	Page
1. Efficiency of Lab-Size Cells and Commercially-Available Modules [11].....	5
2. Chalcogenide Materials for Thin Film Solar Cells [11] .....	9
3. Different Fabrication Methods for CIGS Solar Cells [6].....	10
4. Product Specifications of a Commercial CIGS Cell.....	30
5. Input Parameters for the CIGS Model .....	34
6. Statistical Properties of Absorber Layer Thickness.....	37
7. Case Study1: $I_{sc}$ and $P_{max}$ Output for Different Cell Width .....	41
8. Case Study 2: $I_{sc}$ and $P_{max}$ Output for Different ZnO:Al Thickness .....	41
9. Case Study 3: Overall Power Output in a Given Day.....	41
10. Random Properties for CIGS Solar Cell Model .....	46
11. Iteration History of RBRDO .....	49

## LIST OF FIGURES

Figure	Page
1. Remarkable growth rate of solar PV shown in total world capacity from 1996 -2011 [7].	2
2. Types of solar cell and differences between PV cell, module and array .....	3
3. PV cell, module and array. (Figure is taken from <i>SamlexSolar</i> ) .....	4
4. Scanning Electron Microscopy (SEM) image of a commercial CIGS solar cell.....	7
5. SEM image of a CIGS cell showing typical material used for each layer [12]. .....	11
6. CIGS module interconnect structure [23]. .....	12
7. Illustration of forward current (a) and reverse current (b) in a diode. ....	19
8. I-V curve showing the effect of $R_s$ and $R_{sh}$ [3]. .....	20
9. Different equivalent circuit for modeling of PV cell [27]. .....	22
10. Different equivalent circuit for modeling of PV modules [27]. .....	24
11. I-V curve showing the relationship between individual PV cells and the PV module [38]. .....	26
12. The overview of CIGS modeling process. ....	27
13. The relationship between sunlight irradiation, ambient temperature, and cell temperature in one ideal day. ....	29
14. CIGS geometry input. ....	32
15. I-V Curve .....	33
16. Potential distribution in the CIGS model with $V_{cell}=0V$ (top) and $V_{cell}=1.5V$ (bottom). ..	35
17. Histogram for thickness of CIGS absorber layer .....	36
18. I-V Curve from direct measuring and simulation .....	37

## LIST OF FIGURES (continued)

Figure		Page
19.	Output performance measured in current and power for Case 1 (a-b), Case 2 (c-d) and Case 3(e-f).....	42
20.	RBRDO approach [16] .....	44
21.	Studied multidimensional PV system .....	45
22.	PDF of the mean power output at initial and optimum design .....	48
23.	RBRDO design history .....	50

## LIST OF ABBREVIATIONS

a-Si	Amorphous Silicon
CIGS	Copper Indium Gallium (di)Selenide or $\text{Cu(In,Ga)Se}_2$
CIS	Copper Indium Selenide
CPV	Concentrated/Concentrating Photovoltaic
c-Si	Crystalline Silicon
I-V	Current - Voltage
Mono-Si	Monocrystalline Silicon
MPP	Maximum Power Point
NOCT	Nominal Operating Cell Temperature
PDF	Probability Density Function
Poly-Si	Polycrystalline Silicon
PV	Photovoltaic
P-V	Power - Voltage
RBDO	Reliability-based Design Optimization
RBRDO	Reliability-based Robust Design Optimization
RD	Robust Design
SEM	Scanning Electron Microscopy
SLG	Soda Lime Glass
STC	Standard Test Condition
ZnO:Al	Zinc Oxide (Aluminum(Al) doped)

## LIST OF UNITS

A	Ampere
eV	Electron Volt
J	Joule
m	Meter
s	Second
S	Siemens
sq	Square
V	Volt
W	Watt
$\Omega$	Ohm
K	Kelvin
$^{\circ}\text{C}$	Degree Celsius
C	Coulomb

## LIST OF SYMBOLS

$\mu(x)$	Mean of random parameter X
$\eta$	Efficiency (%)
$\rho$	Electrical resistivity ( $\Omega$ m)
$\sigma$	Conductivity (S/m)
$\beta_{ti}$	Reliability target index
$\tau_{ZnO:Al}$	Transmittance of ZnO:Al layer
$A$	Ideality factor
$C(\cdot)$	Cost function or objective function
$d$	Design variables
$d$	Thickness ( $\mu\text{m}$ )
$E_g$	Band gap (eV)
$FF$	Fill factor
$G(\cdot)$	Performance function
$I$	Net output current (A)
$I_D$	Diode current (A)
$I_L$	Light generated current (A)
$I_{L,in}$	Incident light generated current (A)
$I_{mpp}$	Current at MPP (A)
$I_o$	Saturation current (A)
$I_{oo}$	Initial saturation current (A)

## LIST OF SYMBOLS (continued)

$I_{sc}$	Short circuit current (A)
$J_{L,in}$	Incident light generated current density (A/m <sup>2</sup> )
$J_{oo}$	Initial saturation current density (A/m <sup>2</sup> )
$J_{sc}$	Short circuit current density (A/m <sup>2</sup> )
$k$	Boltzmann's constant (=1.33x10 <sup>-23</sup> J/K)
$k_l$	Temperature coefficient of $I_{sc}$ (A/°C)
$n$	Number of random variables
$nd$	Number of design variables
$np$	Number of probabilistic constraints
$P_{in}$	Power input (W)
$P_{mpp}$	Maximum Power Point (W)
$P_{total}$	Total power output (W)
$q$	Electron charge(=1.5x10 <sup>-19</sup> C)
$R$	Resistance (Ω)
$R_c$	Contact resistance (Ω)
$R_s$	Series resistance (Ω)
$R_{sh}$	Shunt resistance (Ω)
$R_{st}$	Sheet resistance (Ω/sq)
$T_{amb}$	Ambient temperature (K)
$T_c$	Cell temperature (K)

## LIST OF SYMBOLS (continued)

$T_{ref}$	Reference temperature (=298K)
$V_{mpp}$	Voltage at MPP (V)
$V_{oc}$	Open circuit voltage (V)
$w$	Width (mm)
X	Random vectors
$y$	Irradiance (kW/m <sup>2</sup> )

# CHAPTER 1

## INTRODUCTION

For the past centuries, mankind has lived fully dependent on electricity because it allows for more convenience in daily life. This electricity has traditionally come primarily from fossil fuels. Here-in lies the problem; fossil fuels are non-renewable and are generally considered non-environmental friendly. Furthermore, side-products emitted during the burning process of fossil fuels, such as greenhouse gasses or carbon dioxide (CO<sub>2</sub>), lead to air and water pollution, which are indirect causes of the acid rain and global warming. These environmental issues have resulted in the public to look towards green energy as an alternative energy supply, and gradually eliminate the dependency on traditional fossil fuels.

### 1.1 Background and Motivation

Solar energy is known as one of the most promising alternatives to fossil fuels. It is silent, renewable and a non-polluting energy [1]. The conversion of sunlight radiation to electricity is called the photovoltaic (PV) effect. A PV cell, also known as a solar cell, is a device that allows the conversion of sunlight directly into electricity. Although the concept of the PV effect was first introduced in 1839 by Alexandre-Edmond Becquerel, the first modern solar cell was not invented until 1954 at Bell Telephone Laboratories [2-4]. As of today, the PV technology is one of the fastest growing forms of renewable energies, and it is expected to play an important role as a future energy supply. The world's PV power production has been growing exponentially around 30-40% per annum for the past decade [5, 6]. In 2011, the world's total capacity of electricity generated through PV technology reached 70.0 GW, which corresponds to an increase of 75% as compared to end of 2010 as shown in Figure 1.

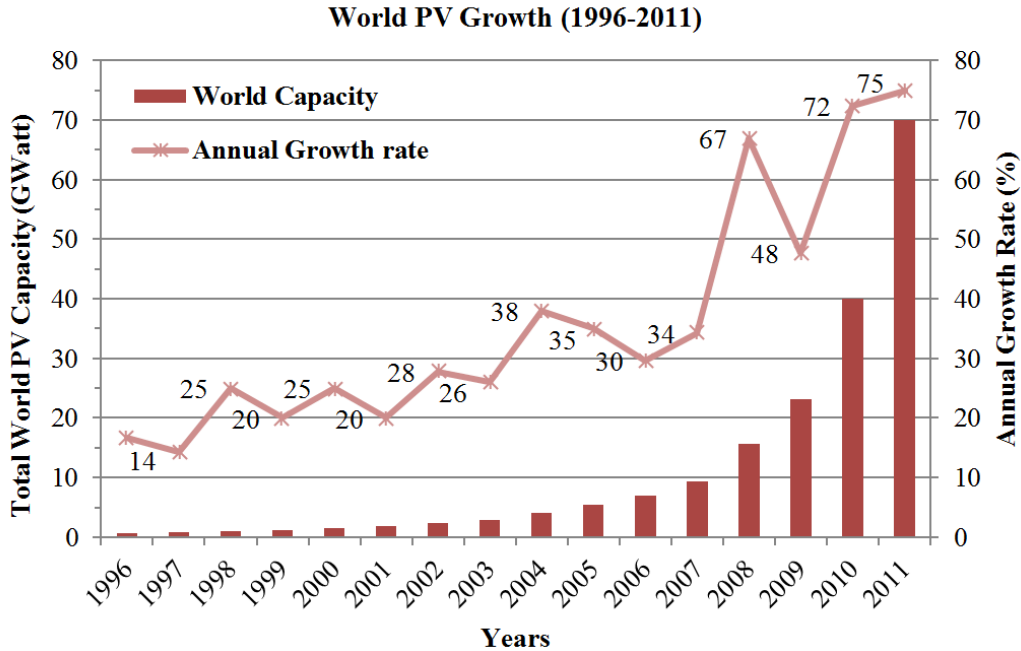


Figure 1. Remarkable growth rate of solar PV shown in total world capacity from 1996 -2011 [7].

### 1.1.1 Background of Solar Cell Technologies

At present, there are a wide range of solar cells that are available on the market. Based on various types of materials and manufacturing technologies, solar cells are usually classified under three generations. The first generation is the wafer-based crystalline silicon (c-Si) solar cells, and has been present for more than 25 years [5]. Monocrystalline (Mono-Si), polycrystalline (Poly-Si) and edge-defined film-fed growth (EFG) ribbon silicon are three main classifications of c-Si, depending on how the wafers are made [4, 8]. The first generation solar cells still dominate around 80% of the solar market due to their high efficiency output, despite the high manufacturing cost and weight. Thin film solar cells are the second generation solar cells, which are significantly cheaper to produce but offer lower efficiency compared to the first generation. Amorphous silicon (a-Si), cadmium telluride (CdTe), copper indium selenide (CIS), and copper indium gallium diselenide (CIGS) are the main types of thin film solar cells that have

been commercially developed [4]. The main advantages of second generation solar cells, along with their low cost, are their flexibility and light weight features. Concentrated/concentrating photovoltaic (CPV), organic solar cells, and dye-sensitized solar cells (DSSC) are the most well-known third generation solar cells. These types of cells are not yet widely commercialized, and are still considered novel concepts under development. The laboratory-scale third generation cells offer a good ratio between electricity produced and cost, and they are believed to surpass the efficiency-cost ratio of first generation solar cells. The properties and performance comparisons between the major PV technologies can be found in Appendix A.

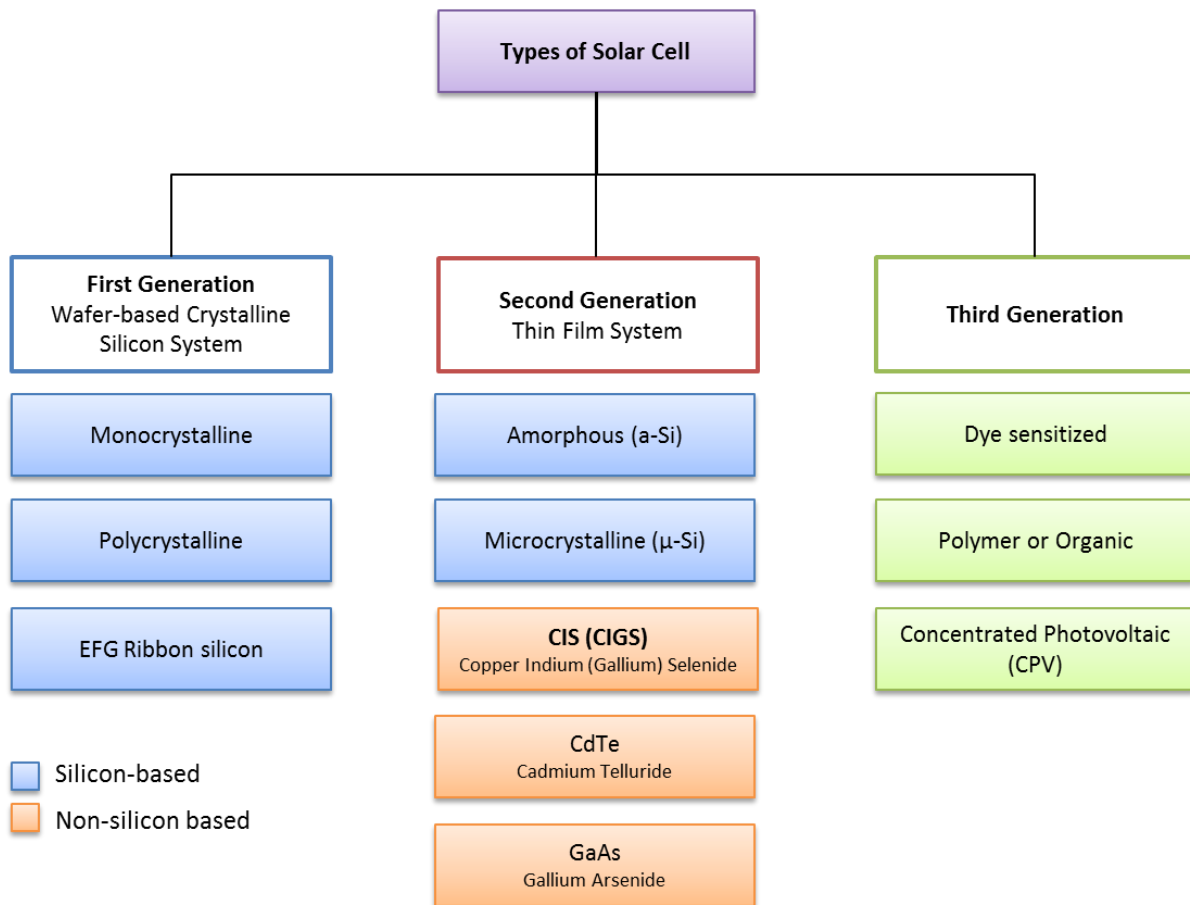


Figure 2. Types of solar cell and differences between PV cell, module and array.

The solar cell is the basic component of a PV system. While a typical 100 cm<sup>2</sup> silicon solar cell produces a reasonable current output (~2.0A), the voltage output (~0.5V) is typically too small for most applications. Thus, in order to produce a voltage output of 12V, between 28 and 36 solar cells are connected together in series and encapsulated into PV modules [8]. The actual number depends on the surface area of each cell. For larger applications like solar roofing or solar power plants, PV modules are linked together to form a PV array.

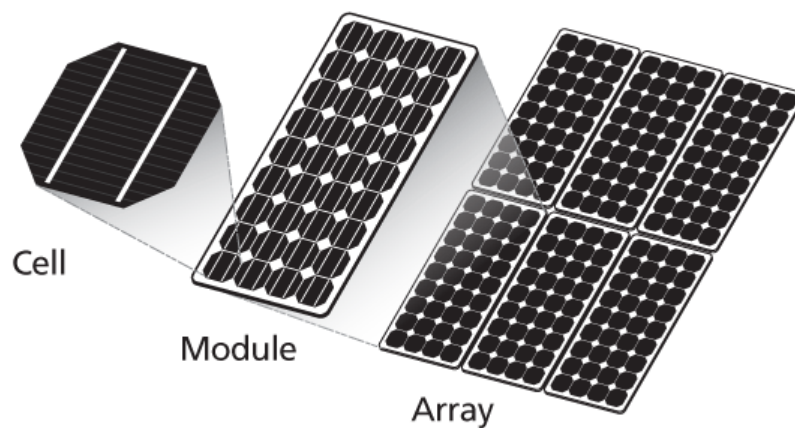


Figure 3. PV cell, module and array. (Figure is taken from *SamlexSolar*)

### 1.1.2 Motivation

Most commercial PV systems in the market come from large-scale manufacturers. Commercial PV systems typically yield lower efficiency when compared with the laboratory PV system (Table 1). For example, the efficiency of CIGS solar modules is in the range of 7-16%, whereas laboratory CIGS cells have demonstrated an efficiency of 20.3%. This is very close to the efficiency of c-Si modules (~14-20%) [4, 9, 10]. The reason for this difference is that the manufacturing variability present during complex large-scale production affects the structure of the solar cells, and further reduces the performance efficiency.

In the laboratory, the environment has been kept in as sterile a condition as possible to prevent any deficiencies during the solar cell production process. As of the time of this study, the prevailing interest within the solar research community is to find ways to improve the performance of commercial solar cells with respect to that of the laboratory solar cells.

TABLE 1  
EFFICIENCY OF LAB-SIZE CELLS AND COMMERCIALY-AVIALABLE  
MODULES [11]

<b>PV material</b>	<b>Commercial module efficiency (%)</b>	<b>Cell efficiency (%)</b>
Thin film-Si	10.4	13.3
CdTe	11.7	17.3
CIGS	12.2	20.3
Poly-Si	16.0	20.4
Mono-Si	20.8	25.0

As with other renewable energies, PV systems depend on nature, which require them to withstand outdoor operating conditions. Depending on geographical region, this may entail extremely harsh conditions. Weather uncertainties and seasonal changes affect the performance of the solar cells. Although manufacturers of commercial PV systems usually give some form of warranty for their products (these can extend up to 20 years), long-hours of exposure in harsh uncertain operating conditions will eventually degrade the performance of the PV systems. Therefore, the desire to ensure the reliability of the commercial PV systems and to avoid any early degradation in the presence of variability and uncertainties (such as manufacturing variability and uncertain operating conditions) has motivated the development of a robustly-designed PV system with high reliability and satiability.

## 1.2 Research Objective and Scope

The scope of this thesis is currently limited to copper indium gallium (di)selenide (CIGS or  $\text{Cu}(\text{In,Ga})\text{Se}_2$ ) solar cells, as the representative of thin film PV technologies. Optimizing the design of commercial CIGS solar cells for reliability and robustness is the main objective of this study. To achieve this objective, there are some key challenges that must be carefully addressed: (1) how to describe the manufacturing variability in the solar cell; (2) how to assess the uncertainty during the operating condition; and (3) how to perform the optimization with limited information of the solar cell.

Although commercial solar cells that come from large-scale manufacturing processes are certified to operate within a certain tolerance, there is still inconsistency observed within the physical structure of the cells. This is because of known complications in producing uniform layers in the large-scale deposition process [12-14]. The physical structure includes thickness of each layer, cell width, and length, and can be used to measure the degree of variability created as a result of the manufacturing process. In the case of CIGS solar cells or most thin-film solar cells, the variability present in the manufacturing process can be signified by the non-uniformity of the deposited CIGS absorber layer [13-15]. Depending on the deposition system, the non-uniformity length scale ranges roughly between 1 cm to 1 m, compared to the size of the deposited device [15]. As a result of the presence of the non-uniform absorber layer, the electric quality output is not the same over the entire area of the CIGS cells [6]. This non-uniform thickness of the CIGS absorber layer can be visualized in Figure 4. There are other more detailed parameters that result from the variability in manufacturing, such as the effect of grain boundaries and the energy band gap inside the cell. These are beyond the scope of this thesis.

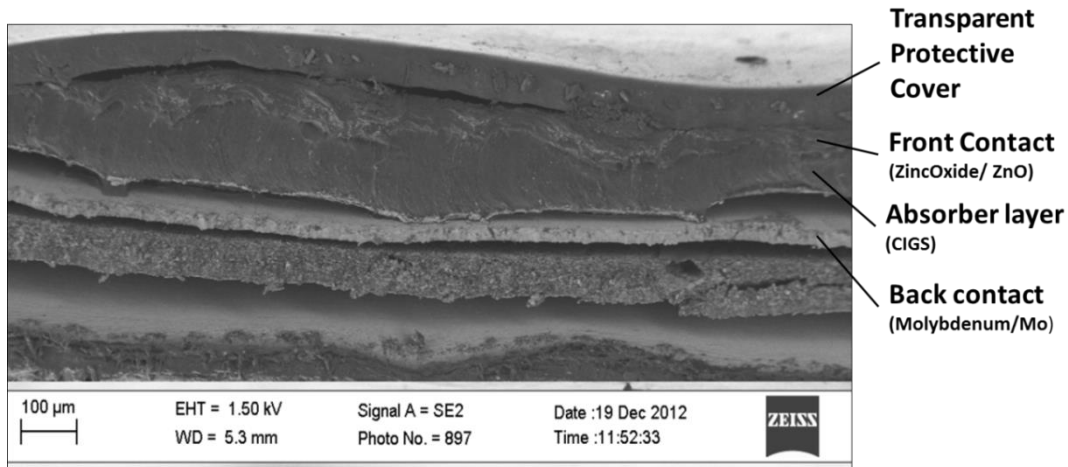


Figure 4. Scanning Electron Microscopy (SEM) image of a commercial CIGS solar cell.

The output of the solar cells depends on the amount of exposure to sunlight. To measure the variability of the operating conditions, the solar irradiance of one ideal day is designed to follow a Gaussian distribution, which will be discussed more in Chapter 2. An ideal day is defined as one where there are no adverse weather effects, such as rain, snow, or clouds, that will inhibit sunlight from reaching the solar cells. In effect, this translates to the availability of the full amount of sunlight over the course of the day; only ideal weather conditions are considered in this thesis. Extreme weather conditions and seasonal changes are outside the scope of this study.

With limited information, design of the solar cell can still be optimized using the reliability-based robust design optimization (RBRDO) approach. RBRDO is not a new approach; it has been used in cases with input uncertainties that were not well defined due to lack of data [16]. RBRDO is essentially an integration of reliability based design optimization (RBDO) and robust design (RD). RBDO characterizes uncertainty variables and failure modes to optimize the designs for higher reliability and RD minimizes the variability without eliminating the source of variation [17].

### **1.3 Thesis Overview**

The main contribution of this thesis is the development of a probabilistic thin film solar cell model that considers the presence of uncertainties in the PV system. A conceptual CIGS solar cell model was first developed in COMSOL Multiphysics 4.2 with material properties of electrical conductivity and geometry of each layer's thickness are taken into account. The uncertainties in manufacturing variability, which are represented as non-uniform thicknesses and uncertain operating conditions, are further introduced into the aforementioned COMSOL model. Finally, the model is optimized using the reliability-based robust design optimization (RBRDO) approach, in order to satisfy the reliability and robustness requirements, while considering these uncertainties.

The rest of the thesis is structured as follows: Chapter 2 reviews the status of the knowledge of CIGS solar cells and parameters required for modeling. Chapter 3 provides detailed information on modeling processes and validation of the CIGS model. Chapter 4 presents the RBRDO framework. In order to prove the feasibility of the proposed approach, the implementation of RBRDO into thin film solar cell design is also demonstrated in Chapter 4. Finally, Chapter 5 summarizes this thesis and also discusses future work.

## CHAPTER 2

### LITERATURE REVIEW

#### 2.1 CIGS Characteristics

$\text{Cu}(\text{In}_{1-x}\text{Ga}_x)\text{Se}_2$ -based thin-film solar cells, often called “CIGS cells”, are chalcogenide-based semiconductor copper indium (di)selenide ( $\text{CuInSe}_2$ , or CIS) solar cells, with the addition of gallium (Ga) alloy [12]. The addition of Ga in the CIS-based solar cells results in the improvement of the device efficiency and electrical properties of the rear contact [12, 18, 19]. CIGS cells currently offer the highest efficiency of around 20% among the thin film technologies [4, 11, 12, 20], although it has been reported that the addition of Ga to CIS could lead to cell deterioration, largely due to grain-interior effects [21]. An efficiency comparison for different types of chalcogenide materials used in thin film technologies is shown in Table 2.

TABLE 2

CHALCOGENIDE MATERIALS FOR THIN FILM SOLAR CELLS [11]

Thin film technologies	Efficiency (%)
CdTe	17.2
$\text{CuInSe}_2$	16.0
$\text{CuGaSe}_2$	10.2
<b><math>\text{Cu}(\text{In,Ga})\text{Se}_2</math></b>	<b>20.3</b>
$\text{Cu}(\text{In,Ga})(\text{S,Se})_2$	17.2*
$\text{CuInS}_2$	11.1
$\text{Cu}(\text{In,Ga})\text{S}_2$	12.0
$\text{Cu}(\text{InAl})\text{Se}_2$	16.9
$\text{Ag}(\text{In,Ga})\text{Se}_2$	9.30
$\text{Cu}(\text{Zn,Sn})(\text{S,Se})_4$	9.60

\* 30cmx30cm sub-module

Different fabrication method for CIGS solar cells are given in Table 3. Effective usage of raw materials leads to lower costs in the manufacturing process, and together with highly stable performance, have made CIGS solar cells economically competitive with c-Si [3, 18]. A major drawback of CIGS is that its energy conversion efficiency tends to be low due to the natural band gap properties that CIGS possess. In order to match the power output of cells in the c-Si group, CIGS cells require a larger operating area to accommodate more cells. This is another disadvantage of CIGS thin-film cells. CIGS cells do have their favorable features. Being thin, flexible and light-weight (unlike c-Si cells which require a heavy glass plate for protection) makes CIGS cells preferable for commercial applications, including residential roofing and photovoltaic-integrated buildings or other structures [12].

TABLE 3  
DIFFERENT FABRICATION METHODS FOR CIGS SOLAR CELLS [6]

<b>Fabrication Methods</b>	
1. Co-evaporation	6. Hybrid evaporation/ sputtering
2. Electrodeposition/selenization	7. Reactive sputtering
3. Electron beam/selenisation	8. Spraying
4. Hybrid selenization	9. Close-spaced vapor transport
5. Sputtering selenization	

CIGS cells are also superior in radiation hardness, meaning that they do not show any degradation under illumination [12, 18]. The factor that contributes most towards CIGS degradation is the combination of high humidity and temperature. High humidity is reported to result in a sharp increase in degradation even at the lowest temperature of (22°C) [22]. Under damp heat exposure, reduction of open circuit voltage ( $V_{oc}$ ) and fill factor ( $FF$ ) are clearly observed, whereas short circuit current density ( $J_{sc}$ ) in CIGS is not severely affected [20, 22, 23].

At present, a low-cost packaging solution that can effectively prevent exposure to moisture so as to maintain CIGS' light-weight and flexible properties is still lacking [20]. Further improvements in energy conversion efficiency and moisture-resistant packaging are important issues that need to be addressed, in order for CIGS to become the cell of choice in PV technology. This will contribute towards the ultimate goal of low-cost, high-reliability renewable energy.

## 2.2 CIGS Solar Cell and Module Structure

CIGS solar cells contain several thin-films which are deposited onto a flexible or ridged substrate [18]. Figure 5 shows the Scanning Electron Microscopy (SEM) image of the cross section of a typical CIGS. Generally, CIGS solar cells are formed using a bottom-up deposition process on a soda lime glass (SLG) [12, 23]. The first layer deposited onto the SLG is typically molybdenum (Mo) back contact, followed by the light absorbing layer of CIGS, a buffer layer that consists of cadmium sulfide (CdS) and a thin layer of high resistivity zinc oxide (ZnO). Lastly, the top front contact that is a transparent layer of aluminum doped zinc oxide (ZnO:Al).

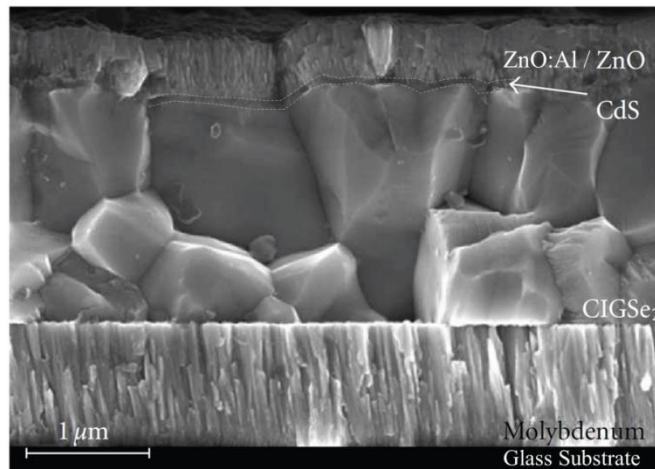


Figure 5. SEM image of a CIGS cell showing typical material used for each layer [12].

Similar with other PV technologies, individual CIGS solar cells can be assembled into any desired module using a manual soldering process. In CIGS technology, the cells can be interconnected in a series connection during the manufacturing process, which is another unique property that distinguishes CIGS technologies from wafer-based cells. Figure 6 shows the interconnect structure consisting of three sections of P1, P2, and P3, which are created from three patterning steps. First, the Mo layer is patterned through laser scribing to separate or create a gap (P1) for the different cells. Second, CIGS, CdS and ZnO layers are deposited on the top of Mo layer, and then patterned to create P2 and further filled by the ZnO:Al layer. Third, a third scribe (P3) is structured down to the Mo layer to finish off the series interconnection. P2 and P3 patterning are carried out using the mechanical scribing [3, 18, 23]. A step by step patterning figure can be found in Appendix B.

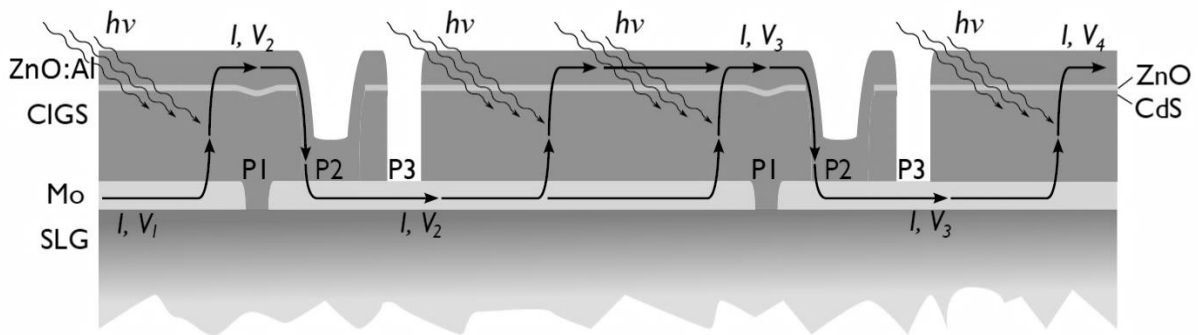


Figure 6. CIGS module interconnect structure [23].

### 2.2.1 ZnO:Al Front Contact

The front contact for CIGS solar cells should fulfill two important requirements: sufficient transparency is necessary to let enough light through to the CIGS absorber layer, and sufficient conductivity is necessary to transport the photo-generated current to the external circuit without excessive resistance losses [12]. To avoid detrimental interdiffusion across the

buffer/absorber (CdS/CIGS) interface, the temperature during the deposition of the front contact should not be higher than 150°C [12]. Most CIGS cells employ radio frequency-sputtered (RF-sputtered) ZnO:Al as the front contact. The relationship between sheet resistance ( $R_{st}$ ), conductivity ( $\sigma_{ZnO:Al}$ ) and thickness ( $d$ ) of the ZnO:Al layer is shown in equation (2.1).

$$R_{st,ZnO:Al} = \frac{1}{d \sigma_{ZnO:Al}} \quad (2.1)$$

The thickness of ZnO:Al is specified to be around 0.3-1.0 $\mu$ m. As the thickness is increased, the conductivity also increases, but the optical transmission of incident light will decrease due to low resistivity. Equation (2.2) describes the transmittance ( $\tau_{ZnO:Al}$ ) as a function of ZnO:Al sheet resistance ( $R_{st,ZnO:Al}$ ) [3, 24].

$$\tau_{ZnO:Al} = \tau_1 - \left( \frac{R_1}{R_{st,ZnO:Al}} \right)^{m_1} \quad (2.2)$$

where  $\tau_1$ ,  $R_1$  and  $m_1$  are constants adjusted to fit experimental data. Experiments to verify these constants had been carried out by previous research in reference [3] and the value obtained for  $\tau_1$ ,  $R_1$  and  $m_1$  are 1, 0.3707, and 0.8226 respectively [3].

### 2.2.2 CdS Buffer Layer

The buffer layer, which typically has a band gap ( $E_g$ ) of between 2.0-3.4eV, is a prerequisite for creating a heterojunction device [3, 6]. Another role of the buffer layer is to protect the electrical properties of the absorber layer against chemical reactions and mechanical damage in subsequent process steps [12, 23]. Omitting the buffer layer resulted in lower efficiency of CIGS [25]. Highest efficiency of CIGS is achieved with the implementation of the CdS buffer layer using chemical bath deposition (CBD) [6, 12]. The thickness of the CdS buffer layer is around 0.05 $\mu$ m. The recent trend has been to substitute CdS with ‘‘Cadmium-free’’ (Cd-

free) wide band gap semiconductors, and to replace the CBD process with a more compatible process in CIGS manufacturing (in-line-compatible) [6, 12].

A highly resistive layer of ZnO with thickness around  $0.1\mu\text{m}$  is sandwiched between the buffer layer and the front contact. The purpose of the ZnO layer is to prevent cell from suffering excessive local electrical losses that may be caused by the non-uniformity of the absorber layer [12]. The ZnO layer helps to isolate the presence of small shunt resistance and recombination due to grain boundaries [23], and eventually it helps to even out the potential across the large-area device.

### **2.2.3 CIGS Absorber Layer**

Excess electron-hole pairs that are generated by the incident light are absorbed by the CIGS layer. Since CIGS has a high absorption coefficient, a layer thickness of approximately  $1.0\text{-}2.5\mu\text{m}$  is sufficient to absorb the maximum irradiation from the sun [3, 6, 12]. A thicker absorber layer also means more material usage, and is typically associated with higher cost. Depending on the deposition technique used, grain boundary and surface roughness will vary, and this will in turn affect the compositional uniformity of the CIGS layer. These are all critical factors that affect the performance of CIGS cells [6].

The band gap of a high performance CIGS solar cell is around  $1.1\text{eV} - 1.2\text{eV}$  [3, 26]. The variation of band gap in CIGS solar cell is expected to have a relation with the amount of Ga concentration that present in the CIGS system [6, 11]. The ideality factor ( $A$ ), depends on the dominant recombination mechanism and it has been demonstrated that the ideality factor for CIGS is between  $1.0 < A < 2.0$  [3, 24, 27]. The conductivity of the CIGS layer is usually observed around  $5 \times 10^{-5} \text{ S/m}$  [3].

#### 2.2.4 Back Contact

Platinum (Pt), gold (Au), silver (Ag), copper (Cu) and molybdenum (Mo) are several metals that have been investigated as possible candidates for the electrical back contact. However, Mo emerged as the preferred metal due to its stability at processing temperature and low contact resistance to CIGS [12]. Mo with thickness  $\sim 0.5\mu\text{m}$ , is typically grown by sputtering or e-beam evaporation process on SLG [3, 6], which is also the first process in most bottom-up manufacturing process for CIGS solar cell.

An interface layer of molybdenum diselenide ( $\text{MoSe}_2$ ) is formed automatically when CIGS is grown onto the Mo layer. This interface layer helps in ohmic transport between CIGS and Mo [6, 12]. A typical value of electrical resistivity of Mo is nearly  $5 \times 10^{-5} \Omega\text{cm}$  or less, and the preferred contact resistivity value is lesser than  $0.3 \Omega\text{cm}$  [3, 12].

#### 2.2.5 Interconnect Structure

The interconnect structure is only present for CIGS modules that are interconnected monolithically during the manufacturing process. The drawback of the interconnect structure is that it affects the performance of the CIGS due to area loss and contact resistance ( $R_c$ ) [3]. At interconnect section (P1-P3) shown in Figure 6, no current is generated, which makes it an inactive part of the CIGS modules. The total width of the interconnect structure is typically about  $300.0 - 400.0\mu\text{m}$  [3].

In the intersection between  $\text{ZnO:Al}$  and Mo, contact resistance ( $R_c$ ) is observed. This contact resistance should be lower than  $0.002 \Omega\text{cm}^2$  [3, 24]. The width of the contact ( $w_c$ ) is about  $50.0\mu\text{m}$ . The effects of poor  $R_c$  can be decreased by widening the contact area [24]. However, this means that the overall active area of the cells have to be sacrificed.

## 2.3 Modeling PV System

PV cells consist of a positive-negative (p-n) junction that is fabricated in a thin film wafer or layer of semiconductor. In CIGS, a heterojunction is formed at the interface between the p-type CIGS absorber layer and n-type CdS/ZnO buffer layer [3]. A PV cell has a characteristic similar to that of a diode in the dark condition (no sunlight exposure) [28].

Photons from the sun that possess energy larger than the CIGS band gap energy are absorbed when PV cells are exposed to sunlight. Since PV cells convert part of the electromagnetic radiation directly to electricity, electron-hole pairs are created proportional to the incident light radiation [29, 30]. In other words, the basic principles of a PV cell can be described as “photons in, electrons out” [8]. It is known that the amount of the photons that are absorbed by the PV cells is not the same as the amount of electrons that flow out the circuit. The energy loss inside the cells is caused by inherent effects such as resistance and recombination, which results in a significantly lower electron output compared to photon input. However, the remaining energy from the photons that is not converted to electricity will result in heating of the cell and will elevate the temperature of the cell [27]. This will in turn affect the performance of the cell. The effect of cell temperature, photocurrent, diode current, and resistance can be used to model the general mechanism of PV cells.

### 2.3.1 Cell Temperature

The temperature inside the PV cell rises up due to the fraction of the sunlight irradiance that is absorbed by the absorber layer (ZnO:Al) but not converted into electricity. This makes the overall cell temperature vary with the solar irradiance and the cell can be expected to operate above the ambient temperature ( $T_{am}$ ) [27]. The cell temperature ( $T_c$ ) can be expressed as the function of solar irradiance ( $y$ ), ambient temperature, and cell condition at NOCT (Nominal

Operating Cell Temperature). NOCT is a standard that defines a normal operating condition at an ambient temperature of 20°C, a solar radiation of 800W/m<sup>2</sup>, and a wind speed of 1m/s. The NOCT condition is obtained from the manufacturer's specification.  $T_c$  is expressed by equation (2.3) [31-33].

$$T_c = T_{am} + \frac{y}{y_{max}} (T_{c,NOCT} - T_{am}) \left( \frac{1 - \eta_{NOCT}}{\tau \alpha} \right) \quad (2.3)$$

where  $T_{c,NOCT}$  is the cell temperature at nominal operating conditions,  $\eta_{NOCT}$  is the cell efficiency at NOCT condition,  $\tau$  is the cover transmittance (if applicable), and  $\alpha$  is cell absorption level. Typically, the efficiency is assumed to be 100% ( $\eta_{NOCT} = 1$ ).

### 2.3.2 Light Generated Current

Light generated current ( $I_L$ ) or photocurrent depends primarily on the variation of the temperature inside the cells ( $T_c$ ) the irradiation ( $y$ ) around the cell, which can be expressed as equation (2.4) [27, 31, 32, 34, 35].

$$I_L = \left[ I_{sc} + k_I (T_c - T_{ref}) \right] \frac{y}{y_{ref}} \quad (2.4)$$

where  $I_{sc}$  is short circuit current,  $k_I$  is  $I_{sc}$  temperature coefficient of the cell,  $T_{ref}$  is reference temperature (25°C), and  $y_{ref}$  is irradiance at reference condition (1000W/m<sup>2</sup>). The reference condition is mostly referred to the Standard Testing Condition (STC). STC specifies testing temperature at 25°C, an irradiance of 1000W/m<sup>2</sup>, and with an air mass 1.5 (AM1.5) spectrum [34]. The temperature coefficient of  $I_{sc}$  ( $k_I$ ), can be obtained either from the manufacturer specification data or calculated from the equation (2.5) [28, 30].

$$k_I = \frac{I_{sc(T_2)} - I_{sc(T_1)}}{(T_2 - T_1)} \quad (2.5)$$

where  $I_{sc(T_2)}$  and  $I_{sc(T_1)}$  is the short circuit current at cell temperature ( $T_1$ ) and ( $T_2$ ) respectively. For simplification, either STC or NOCT are used as the reference condition for  $T_1$  or  $T_2$ .

If the transmission effect of the incident light generated ( $I_{L,in}$ ) though the transparent front contact is taken into account,  $I_L$  can also be expressed as equation (2.6).

$$I_L = \tau I_{L,in} \quad (2.6)$$

In CIGS, the front contact is the ZnO:Al layer. The effect of the transmission though ZnO:Al layer ( $\tau_{ZnO:Al}$ ) is shown in equation (2.2). A more accurate value of  $I_{L,in}$  should be obtained from experiment. However, depending on the area,  $I_{L,in}$  can be calculated by multiplying incident current density ( $J_{L,in}$ ) and the exposed surface area. Incident light generated current density ( $J_{L,in}$ ) has a typical value of 350A/m<sup>2</sup> at STC [3].

### 2.3.3 Diode Current

Diode current ( $I_D$ ) describes the current-voltage behavior at p-n junction.  $I_D$  is a function of diode saturation current ( $I_o$ ), ideality factor ( $A$ ), applied voltage ( $V$ ), and cell temperature ( $T_c$ ), and is mathematically shown in equation (2.7) [2, 3].

$$I_D = I_o \left[ e^{\left(\frac{qV}{AkT_c}\right)} - 1 \right] \quad (2.7)$$

where  $q$  and  $k$  are the electron charge and  $k$  is the Boltzmann's constant.

The diode saturation current ( $I_o$ ), also called reverse saturation current, is the small amount of current that flows in the reverse direction (Figure 7b).  $I_o$  is constant under constant temperature. As mentioned before, the temperature inside the cell varies with solar irradiance

(section 2.3.1), so  $I_o$  also depends on temperature. Considering the temperature inside the PV cells,  $I_o$  can be expressed by equation (2.8) and equation (2.9).

$$I_o = I_{oo} \left( \frac{T_1}{T_2} \right)^3 e^{\frac{qE_g}{Ak \left( \frac{1}{T_1} - \frac{1}{T_2} \right)}} \quad (2.8)$$

$$I_{oo} = \frac{I_{sc}}{e^{\left( \frac{qV_{oc}}{kAT_1} \right)} - 1} \quad (2.9)$$

$I_{oo}$  is the initial saturation current at  $T_1$ .  $T_1$  is generally taken as the reference temperature at STC (25°C).  $T_2$  is the cell temperature.  $E_g$  is the band gap of the semiconductor materials (for CIGS,  $E_g = 1.1$ -1.2eV).  $I_{sc}$  and  $V_{oc}$  can be obtained from manufacturer specification. By ignoring the small diode effect and ground-leakage current with zero-terminal voltage, the  $I_{sc}$  can be approximated to be equal to  $I_L$  [2, 29, 31].

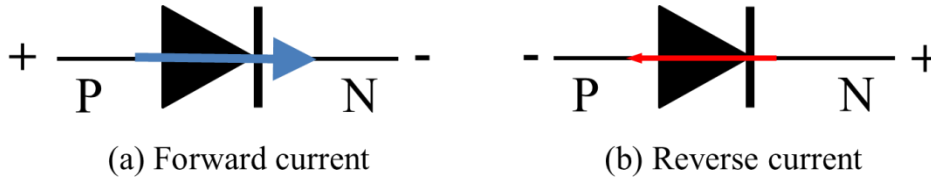


Figure 7. Illustration of forward current (a) and reverse current (b) in a diode.

### 2.3.4 Resistance and Conductivity

Two main resistances that exist in the PV system are series resistance ( $R_s$ ) and shunt resistance ( $R_{sh}$ ). These resistances affect the output performance of the solar cell output as shown in Figure 8. Series resistance ( $R_s$ ) represents the internal losses due to current flow and also due to wiring connection [28, 36]. In CIGS solar cells,  $R_s$  is caused by the bulk resistance of the semiconductor material [3].  $R_s$  causes reduction in  $FF$  and  $I_{sc}$  and the effect of  $R_s$  becomes more apparent in a PV module that consists of many series connected cells, because the  $R_s$  is

multiplied by the number of cells connected in series [2].  $R_s$  contributes to define the effect of the Maximum Power Point (MPP) and open-circuit condition in a Current – Voltage (I-V) curve [28, 36].

Shunt resistance ( $R_{sh}$ ), also called parallel resistance, is parallel with the diode.  $R_{sh}$  corresponds to the leakage current to electrical ground, which results in power output losses [28, 36]. This type of resistance is mainly due to manufacturing defects, rather than poor design of the solar cell. For example, in CIGS,  $R_{sh}$  is caused by partial shorting of cells near the edges and also between two adjacent cells through CIGS in the P1 scribe [3].  $R_{sh}$  acts to define the slope characteristics near the short-circuit condition in I-V curve [36]. The PV system’s efficiency is sensitive to small changes in  $R_s$  but insensitive to the variation in  $R_{sh}$ , so it is commonly neglected [27, 28]. In an ideal solar cell system,  $R_s$  and  $R_{sh}$  are commonly assumed to have no effect on the PV system,  $R_s = R_{sh} = 0$  [28].

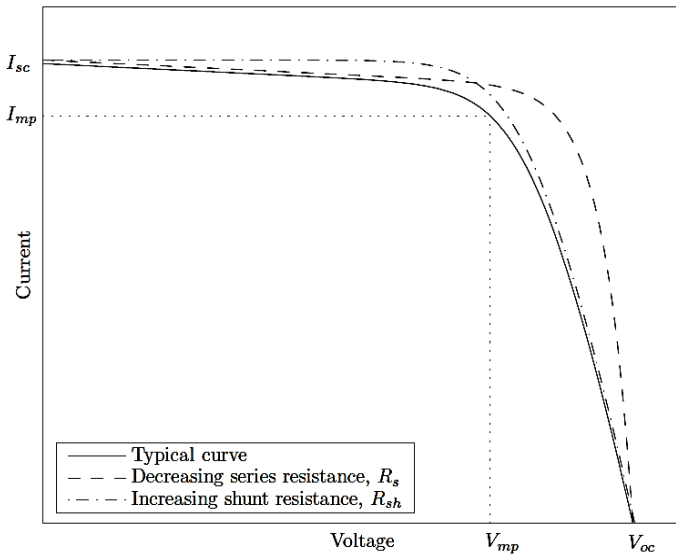


Figure 8. I-V curve showing the effect of  $R_s$  and  $R_{sh}$  [3].

The resistance ( $R$ ) of a material can be obtained from equation (2.10).

$$R = \rho \frac{l}{Area} = \rho \frac{l}{w d} \quad (2.10)$$

where  $\rho$  is the electrical resistivity ( $\Omega\text{m}$ ),  $l$  is the material length (m).  $Area$  is the cross sectional area ( $\text{m}^2$ ), which is equal to the width ( $w$ ) and thickness ( $d$ ). For semiconductor materials,  $\rho$  is also the inverse of the conductivity ( $\sigma$ ), as shown in equation (2.11).

$$\rho = \frac{1}{\sigma} \quad (2.11)$$

$R_{st}$  is a measure of the electrical resistance of a thin film that has a uniform thickness ( $d$ ) [3]. Combining the resistivity of a material and the thickness, sheet resistance ( $R_{st}$ ) can be obtained from equation (2.12).

$$R_{st} = \frac{\rho}{d} \quad (2.12)$$

### 2.3.5 Modeling PV Cells

There are different methods in modeling a PV cell. The equivalent circuits that show the differences in modeling a PV cell are shown in Figure 9. The equivalent circuits consist of an input of current source ( $I_L$ ), which is placed in parallel with an ideal diode ( $D_1$ ) [2, 28].  $I_L$  represents the current that is generated by the incident light or photons from sunlight exposure. While  $D_1$  simulates the diffusion process of the carriers moving towards the depletion region,  $D_2$  represents the recombination that happens in the space charge section of the PV junction [36]. Recombination typically occurs when PV cells lose the electron-hole pairs, which mostly happens due to impurities in the PV structure. The result of recombination is reduction in both current and voltage. Recombination is usually classified based on the region of the cell in which

it occurs, such as surface, bulk materials, or depletion region [2]. The difference between each model depends on how many factors are considered in the model.

The general equivalent circuit model (Figure 9a) is also known as the one-diode model or single-diode model. The effect of series resistance ( $R_s$ ) and shunt resistance ( $R_{sh}$ ) in the one-diode model are taken into account, whereas sometimes they are omitted for simplification purposes. Figure 9c shows the simplified equivalent circuit model, where  $R_s$  and  $R_{sh}$  are assumed to be negligible ( $R_s = R_{sh} = 0$ ). This simplified model is also known as ideal PV system. The additional effect of recombination ( $D_2$ ) is considered for the more accurate equivalent circuit model (Figure 9d). This model is also called the two-diode or double-diode model. Since PV system is typically more sensitive to small variations in  $R_s$  but less prone to variations in  $R_{sh}$ , so  $R_{sh}$  is commonly neglected [27, 28]. The appropriate equivalent circuit for this particular system is shown in Figure 9b, which only studies the effect of  $R_s$ , and omits the effect of  $R_{sh}$ .

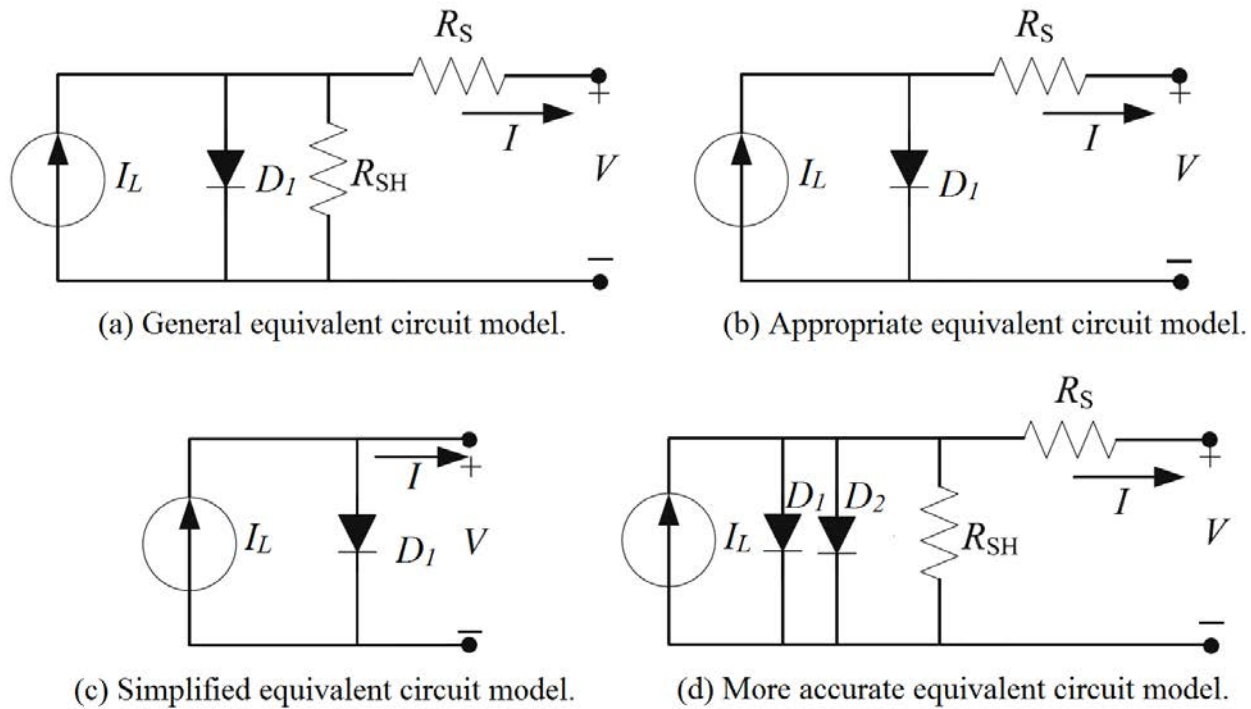


Figure 9. Different equivalent circuit for modeling of PV cell [27].

The net output current ( $I$ ) for PV cells is obtained by applying Kirchhoff's current law (KCL) and ohm's law on the equivalent circuit shown in Figure 9. A more detailed explanation of KCL and Ohm's Law is provided in Appendix C.

$$I = I_L - I_D - I_R \quad (2.13)$$

where  $I_L$  is the light generated current,  $I_D$  is the diode current and  $I_R$  is the current associated with the presence of  $R_s$  and  $R_{sh}$ . For each model, the net output current is:

(a) General equivalent circuit model [3, 27, 34]:

$$I = I_L - I_o \left[ e^{\left( \frac{q(V+IR_s)}{AkT_c} \right)} - 1 \right] - \frac{V + IR_s}{R_{sh}} \quad (2.14)$$

(b) Appropriate equivalent circuit model [28, 29, 37]:

$$I = I_L - I_o \left[ e^{\left( \frac{q(V+IR_s)}{AkT_c} \right)} - 1 \right] \quad (2.15)$$

(c) Simplified equivalent circuit model [10, 27]:

$$I = I_L - I_o \left[ e^{\left( \frac{qV}{AkT_c} \right)} - 1 \right] \quad (2.16)$$

(d) More accurate equivalent circuit model [2, 36]:

$$I = I_L - I_{o_1} \left[ e^{\left( \frac{q(V+IR_s)}{AkT_c} \right)} - 1 \right] - I_{o_2} \left[ e^{\left( \frac{q(V+IR_s)}{AkT_c} \right)} - 1 \right] - \frac{V + IR_s}{R_{sh}} \quad (2.17)$$

### 2.3.6 Modeling PV Modules and PV Plants

In reality, PV cells are connected in series or parallel in a module or array in order to generate required power output. The different equivalent circuits for PV modules that arrange cells in parallel and series branches are shown in Figure 10.  $N_p$  is the number of cells connected in parallel and  $N_s$  is the number of cells connected in series. Considering number of cells connected in series ( $N_s$ ) and in parallel ( $N_p$ ), the current, voltage and resistances of PV module can be numerically represented in equation (2.18), with the similar scaling also applicable to  $I_L$ ,  $I_o$ ,  $I_{sc}$  and  $V_{oc}$  [36].

$$\begin{aligned}
 I_{\text{module}} &= N_p \cdot I_{\text{cell}} & R_{s, \text{module}} &= \frac{N_s}{N_p} \cdot R_{s, \text{cell}} \\
 V_{\text{module}} &= N_s \cdot V_{\text{cell}} & R_{\text{sh, module}} &= \frac{N_s}{N_p} \cdot R_{\text{sh, cell}}
 \end{aligned}
 \tag{2.18}$$

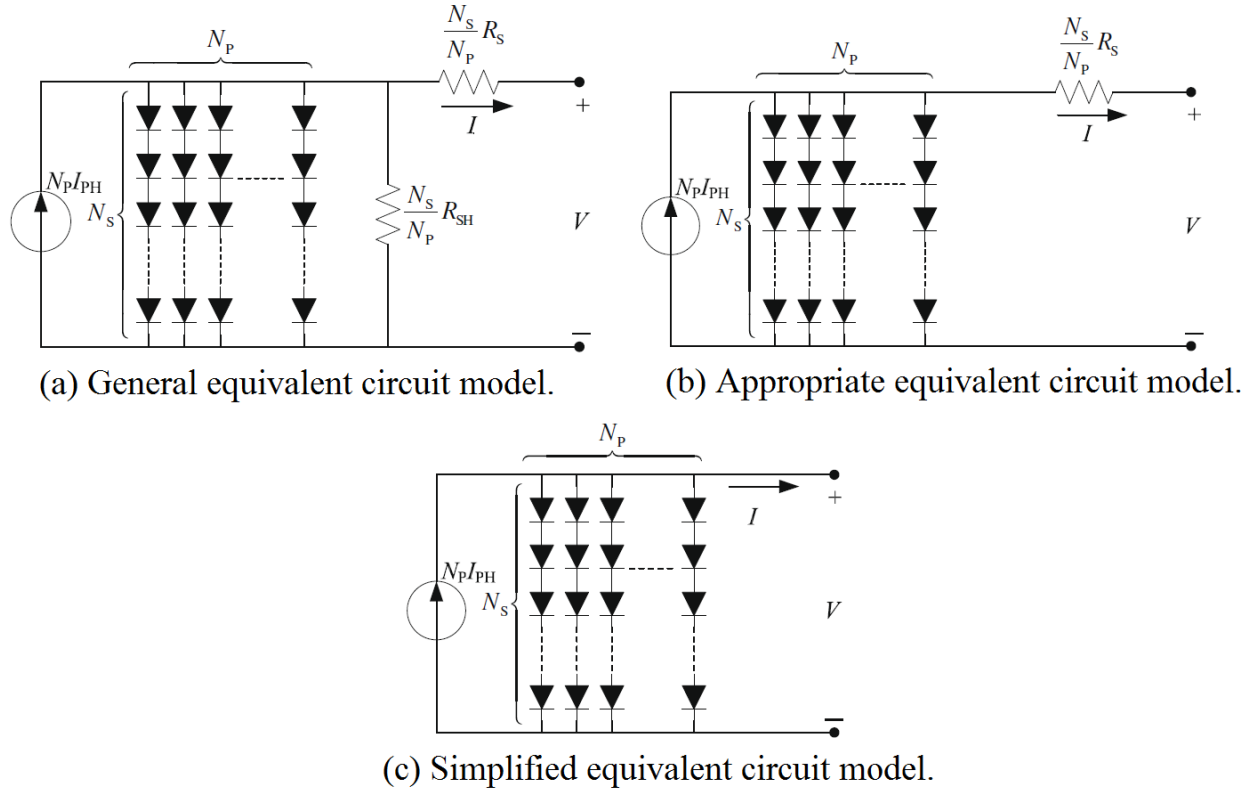


**Figure 10.** Different equivalent circuit for modeling of PV modules [27].

The net output current ( $I$ ) for PV modules, which is shown in Figure 10, can be expressed by equation (2.19) – (2.21) [27].

(a) General equivalent circuit model:

$$I = N_p I_L - N_p I_o \left[ e^{\left( \frac{q}{AkT_c} \left( \frac{V + IR_s}{N_s + I \frac{R_s}{N_p}} \right) \right)} - 1 \right] - \frac{\frac{N_p}{N_s} V + IR_s}{R_{sh}} \quad (2.19)$$

(b) Appropriate equivalent circuit model:

$$I = N_p I_L - N_p I_o \left[ e^{\left( \frac{q}{AkT_c} \left( \frac{V + IR_s}{N_s + I \frac{R_s}{N_p}} \right) \right)} - 1 \right] \quad (2.20)$$

(c) Simplified equivalent circuit model:

$$I = N_p I_L - N_p I_o \left[ e^{\left( \frac{qV}{AkT_c} \right)} - 1 \right] \quad (2.21)$$

When cells are connected in series, the overall voltage performance is affected. This is because the module's voltage is equal to the product of the number of cells connected in series and the voltage of an individual cell, as shown in equation (2.18). The current of the module remains unchanged in series-connected system, and is the same as the current of an individual cell. On the other hand, when cells are connected in parallel, the module current increases in proportion to the number of cells connected in parallel (equation (2.18)). In parallel-connected system, the voltage remains the same as the voltage of an individual cell. Figure 11 shows the relationship between the number of cells connected in series or parallel in the I-V curve.

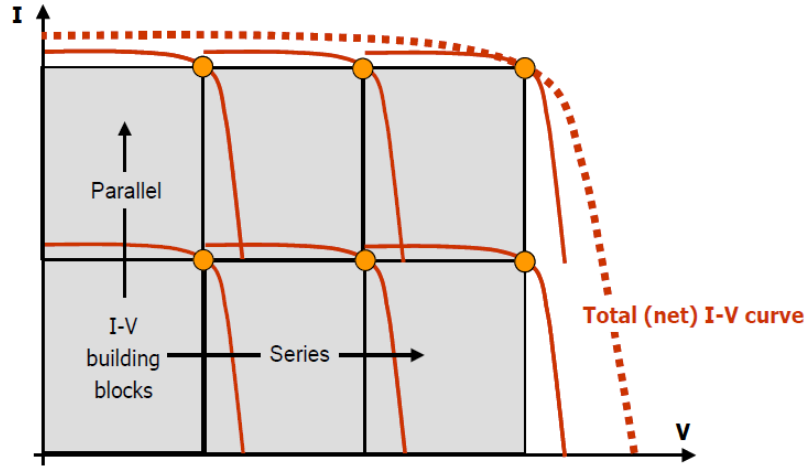


Figure 11. I-V curve showing the relationship between individual PV cells and the PV module [38].

Scaling up from an individual PV cell to a PV module can also be implemented to simulate any array or any larger PV plant that is composed of  $n$  number of parallel ( $N_{parallel}$ ) sub-systems. Each sub-systems should consists of  $n$  number ( $N_{series}$ ) of PV panels connected in series [36]. Mathematically, the scaling from PV panels to a PV plant is shown in equation (2.22).

$$\begin{aligned}
 I_{plant} &= N_{parallel} \cdot I_{panel} & R_{s, plant} &= \frac{N_{series}}{N_{parallel}} \cdot R_{s, panel} \\
 V_{plant} &= N_{series} \cdot V_{panel} & R_{sh, plant} &= \frac{N_{series}}{N_{parallel}} \cdot R_{sh, panel}
 \end{aligned}
 \tag{2.18}$$

## CHAPTER 3

### MODELING APPROACH

#### 3.1 Overview of Modeling Approach

The development process of CIGS modeling will be covered in detail in this chapter. The general block diagram of the proposed modeling approach is shown in Figure 12. The inputs for the CIGS model are irradiance, ambient or surrounding temperature, and external voltage. The outputs of the model are currently limited to power and current. In the future, the efficiency and fill factor will be considered as the output parameters.

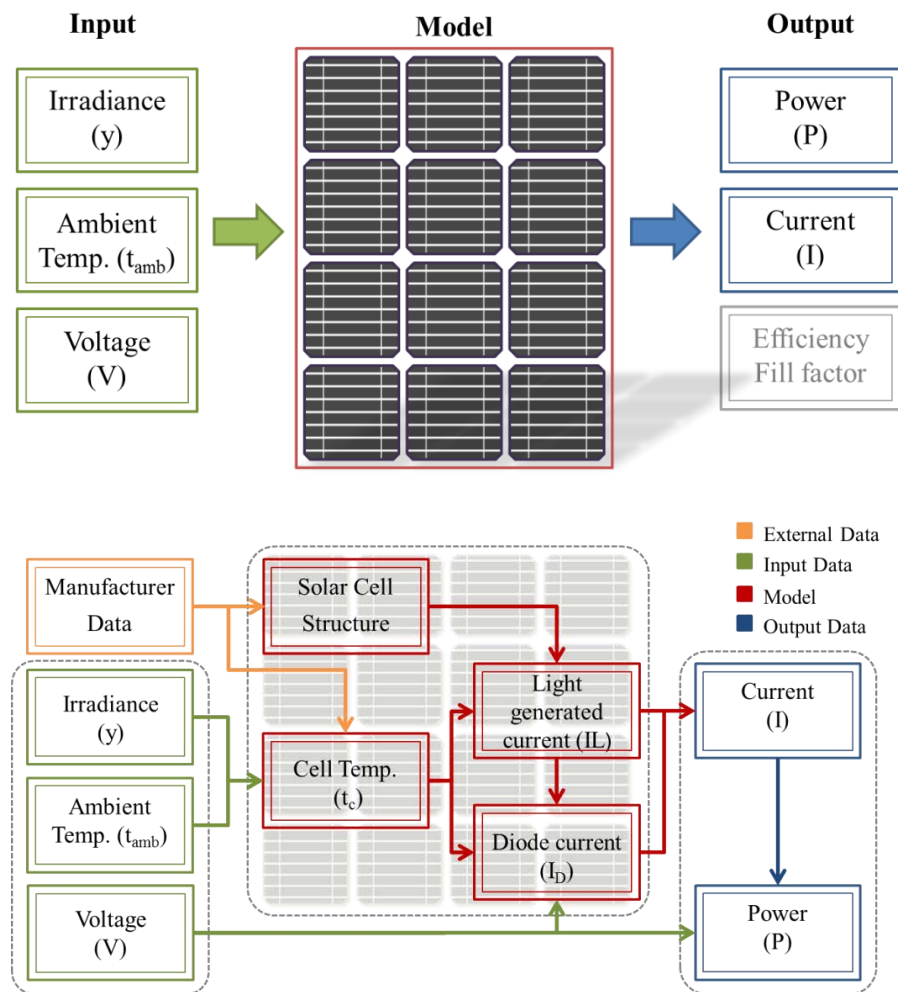


Figure 12. The overview of CIGS modeling process.

## 3.2 Input Parameters

The input parameters for the solar cell models are the operating conditions, the external voltage and also the cells' characteristics that are obtained from the manufacturer's data. Operating conditions and external voltage can be adjusted in order to study how these parameters can contribute to the overall performance of the solar cells. Ranging the external voltage is essential to find the complete I-V characteristics. Since this study focuses on commercial solar cells, the specifications and data provided by the manufacturer are taken to be accurate and used as-is without modification.

### 3.2.1 Operating Conditions

There are two main operating conditions that are considered in the modeling process: the irradiance from sunlight exposure and the ambient/surrounding temperature of the solar cells. Solar irradiance is defined as the amount of radiant energy received from the sun per unit area within a certain time period [8]. For the purpose of simulating an outdoor operating condition that closely mimics reality, the solar radiation intensity for a normal day is assumed to follow a Gaussian distribution. The simulated operating condition for a day is assumed to be an ideal weather condition, where any seasonal changes and extreme temperature fluctuations are not taken into account. The Gaussian equation used to generate the irradiance ( $y$ ) in one sample day are shown in equation (3.1) [27].

$$y(x) = y_{\max} e^{-\frac{(x-x_a)^2}{2b^2}} \quad (3.1)$$

where  $y_{\max}$  is the maximum sunlight irradiance that occurs at the given time ( $x_a$ ), and  $b$  is the standard deviation of the Gaussian function. Figure 13 shows the Gaussian distribution plot for

irradiance for a 24-hour period of time (1 day), where the condition of  $y_{max} = 1 \text{ kW/m}^2$  occurs at 12 pm (noon),  $x_a = 12$ , and  $b = 2$ .

Similar to sunlight irradiance, the ambient temperature ( $T_{amb}$ ) is also assumed to follow the Gaussian distribution with the reference temperature ( $T_{ref}$ ) of  $25^\circ\text{C}$ . The maximum ambient temperature is set to be  $35^\circ\text{C}$  at noon shown in Figure 13. Both irradiance and ambient temperature have a direct effect on cell temperature. This is shown in equation (2.3).

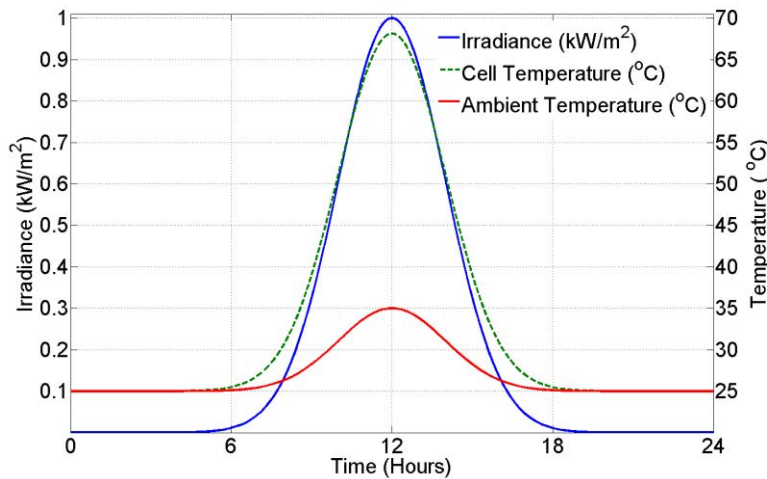


Figure 13. The relationship between sunlight irradiation, ambient temperature, and cell temperature in one ideal day.

### 3.2.2 Manufacturer Specifications

As mentioned previously, the manufacturer specifications are also used in determining the model's parameters. Table 4 shows the specification for a typical low-cost CIGS commercial cell. The most important parameters which are widely used for measuring the cell electrical performance are  $V_{oc}$  and  $I_{sc}$  [27]. Given the PV cell's  $V_{oc}$  and  $I_{sc}$ , the initial diode saturation current ( $I_{00}$ ) at reference temperature can be approximately obtained using equation (2.9).

TABLE 4

PRODUCT SPECIFICATIONS OF A COMMERCIAL CIGS CELL

Characteristics	Specifications
Short circuit current ( $I_{sc}$ )	0.5A
Open circuit voltage ( $V_{oc}$ )	15.6V
Temperature coefficient for power, voltage, current ( $k$ )	-0.5%/°C
Maximum power ( $P_{max}$ )	6.5W

\* Data at STC, (1000W/m<sup>2</sup>), spectrum 1.5AM, and cell temperature 25°C

### 3.3 Output Parameters

Output parameters are important factors in determining the characteristics of a PV system. These factors are as follows:

- Net current output,  $I$ , which is defined by equation (2.13).
- Power output,  $P$ , which is the product of current and voltage. At the time of writing, only and power output is the main output parameters considered.

$$P = I \times V \quad (3.2)$$

- Fill factor,  $FF$ , which is the ratio of the actual maximum power point (MPP) at the nominal operating condition ( $P_{mpp}$ ) to the product of  $V_{oc}$  and  $I_{sc}$ .

$$FF = \frac{P_{mpp}}{V_{oc} I_{sc}} = \frac{V_{mpp} I_{mpp}}{V_{oc} I_{sc}} \quad (3.3)$$

where  $V_{mpp}$  is the voltage at MPP,  $I_{mpp}$  is the current at MPP.

- Efficiency,  $\eta$ , is the energy conversion efficiency which is the ratio between the generated power at MPP and total power of the incident light input [3].

$$\eta = \frac{P_{mpp}}{P_{L,in}} = \frac{V_{oc} I_{sc} FF}{P_{L,in}} \quad (3.4)$$

### 3.4 CIGS Modeling

The steady state electrical conduction equation is governed by the continuity equation with the time derivative of charge density equal to zero [23]. Employing Ohm's law, material properties of the electrical conductivity ( $\sigma$ ) are incorporated with current density,  $J = \sigma E$ .  $E$  is the electrical field and can be determined by the gradient of the potential energy,  $E = -\nabla V$ . COMSOL Multiphysics is utilized to solve the resulting partial differential equation (3.5).

$$\begin{aligned}\nabla \cdot J - \frac{\delta \rho}{\delta t} &= 0 \\ \nabla(\sigma E) &= 0 \\ \nabla(\sigma \nabla V) &= 0\end{aligned}\tag{3.5}$$

Apart from solving equation, this software packages also handles geometry modeling and meshing of the structure. The 2D CIGS model is built in COMSOL Multiphysics 4.2 and integrated with MATLAB R2010a. The structure of the cell (width, length, and thickness of each layer) and the material properties (conductivity and transmittance of ZnO:Al), as described in Section 2.2, are used in the model. The basic mechanism of the CIGS cell is modeled by implementing the information in Section 2.3.

#### 3.4.1 Solar Cell Geometry Input

The CIGS model geometry is created for a single cell, with the interconnect structure. A typical CIGS solar cell structure is developed with the input geometry and dimensions shown in Figure 14. Three thickness structures are modeled: aluminum zinc oxide (ZnO:Al) as the transparent front contact, CIGS absorber layer, and Molybdeum (Mo) back contact. The glass substrate is not modeled, but the interconnect sections of 0.5mm width are modeled. Since the buffer layer is significantly smaller than the other layers, the cadmium sulfide (CdS) buffer layer

is modeled as a boundary instead of a section. The plane length of the solar cell module equals to the length of the CIGS cell, which is taken to be 10.0cm.

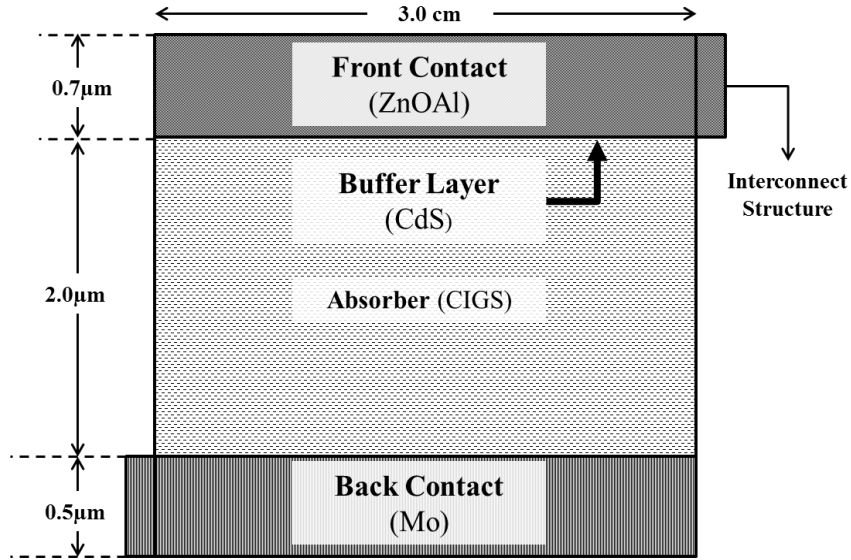


Figure 14. CIGS geometry input.

### 3.4.2 Model Implementation

The implementation of the model is done using Electric Current (ec) physics that comes as part of the COMSOL package. The boundary conditions are set as follows:

- The initial value of electric potential is set to be zero ( $V=0$ )
- Ground boundary condition ( $V=0$ ) is specified for the front and back contact interconnect area, as this area is an inactive area of the cell.
- Electric potential boundary condition is set as  $V_{cell}$ .  $V_{cell}$  is an adjustable parameter and is further varied from 0 - 2.0V when running the simulation.
- At the interface between each layer, the interior boundaries are set to be continuous:  $n_2 \cdot (J_2 - J_1) = 0$ . The conductivity and other important input parameters are listed in Table 5.

- Normal current density ( $-n.J=J_{in}$ ) occurs on the outer layer of the front contact.
- Insulation boundary condition ( $-n.J=0$ ), which specifies no current flow across the boundary, is set for the other outer boundaries of the cell.

Meshing the CIGS geometry is done using the default setting. The parametric sweep feature is implemented in order to vary the applied voltage. The model is solved using the nonlinear parametric solver. COMSOL Multiphysics has a graphical user interface, and it also features livelink integration with MATLAB. This enables scripting in MATLAB and allows COMSOL to engage MATLAB or vice versa. The results when voltage is set to  $V_{cell}=0V$  and  $V_{cell}=1.5V$  are shown in Figure 16. The current is generated at the front contact and slowly being consumed at the interconnect area. Current is channeled and collected at the interconnect area before being transferred to the next cell. The I-V curve for this particular model is shown in Figure 15. Although the results show that the potential distribution reached saturation at  $V_{cell}=1.5V$ , an experimental approach is still required to verify this result.

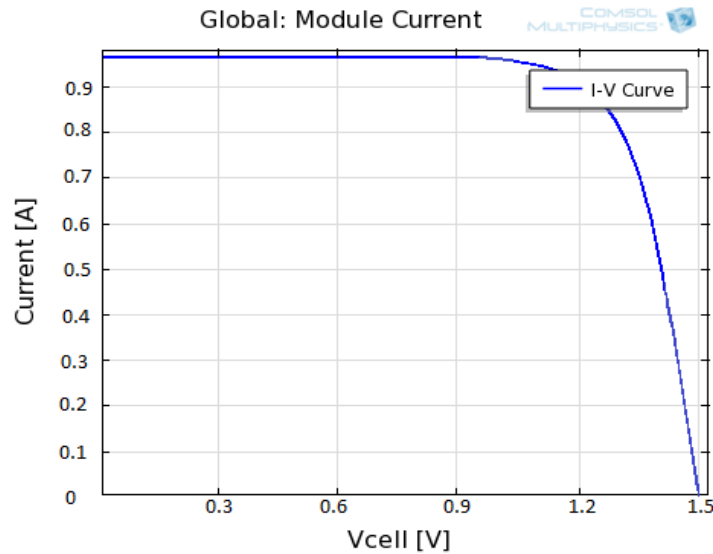


Figure 15. I-V Curve.

TABLE 5  
INPUT PARAMETERS FOR THE CIGS MODEL

Parameters	Symbol	Value
Cell width	$w_c$	3.0 cm
Cell length	$l_c$	10.0 cm
Thickness of CIGS absorber	$d_{CIGS}$	2.0 $\mu\text{m}$
Thickness of ZnO:Al	$d_{ZnO:Al}$	0.7 $\mu\text{m}$
Thickness of Mo	$d_{Mo}$	0.5 $\mu\text{m}$
Interconnect width	$w_{int}$	0.5mm
ZnO:Al conductivity*	$\sigma_{ZnO:Al}$	$4.5 \times 10^4$ S/m
CIGS conductivity*	$\sigma_{CIGS}$	$5.0 \times 10^{-5}$ S/m
Mo Conductivity*	$\sigma_{Mo}$	$3.1 \times 10^6$ S/m
ZnO:Al transmission	$\tau_{ZnO:Al}$	Equation (2.2)
Resistance	$R_{ZnO:Al}/R_{CIGS}/R_{Mo}$	Equation (2.9) and (2.10)
CIGS band gap	$E_g$	1.2 eV
Ideality factor	$A$	1.2
Reference temperature	$T_{ref}$	25°C or 298K
Initial light generated current density	$J_{L,in}$	350 A/m <sup>2</sup>
Initial saturation current density	$J_{oo}$	$1.0 \times 10^6$ A/m <sup>2</sup>
Light generated current	$I_L$	Equation (2.5)
Diode current	$I_D$	Equation (2.6)
Net current output	$I$	Equation (2.12)

\* The value is taken based on the previous experiment done in [3].

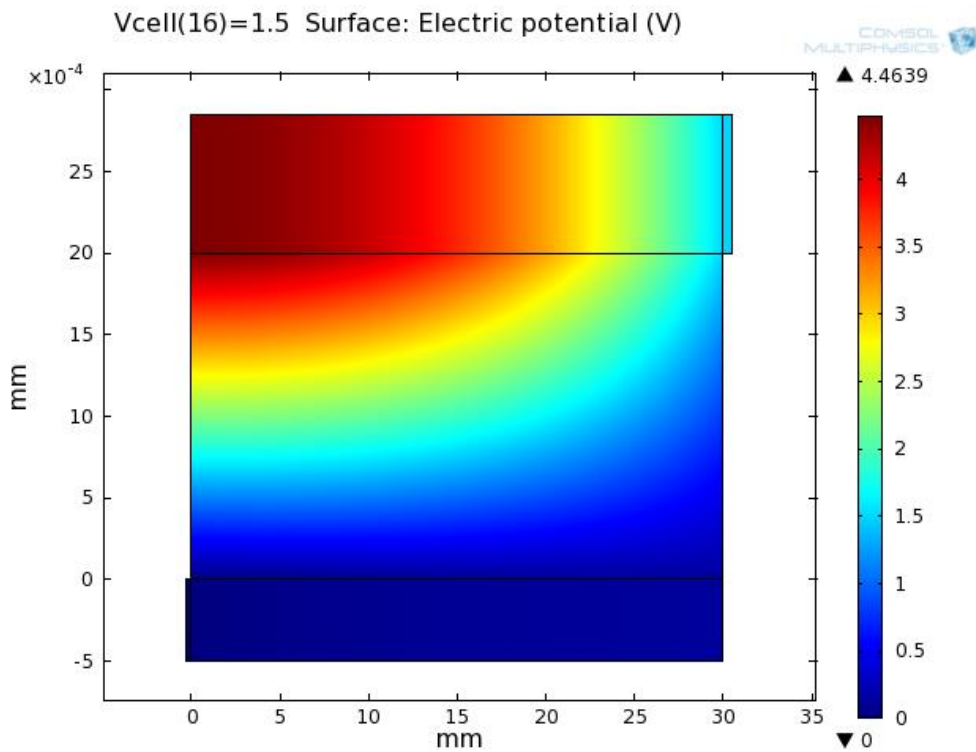
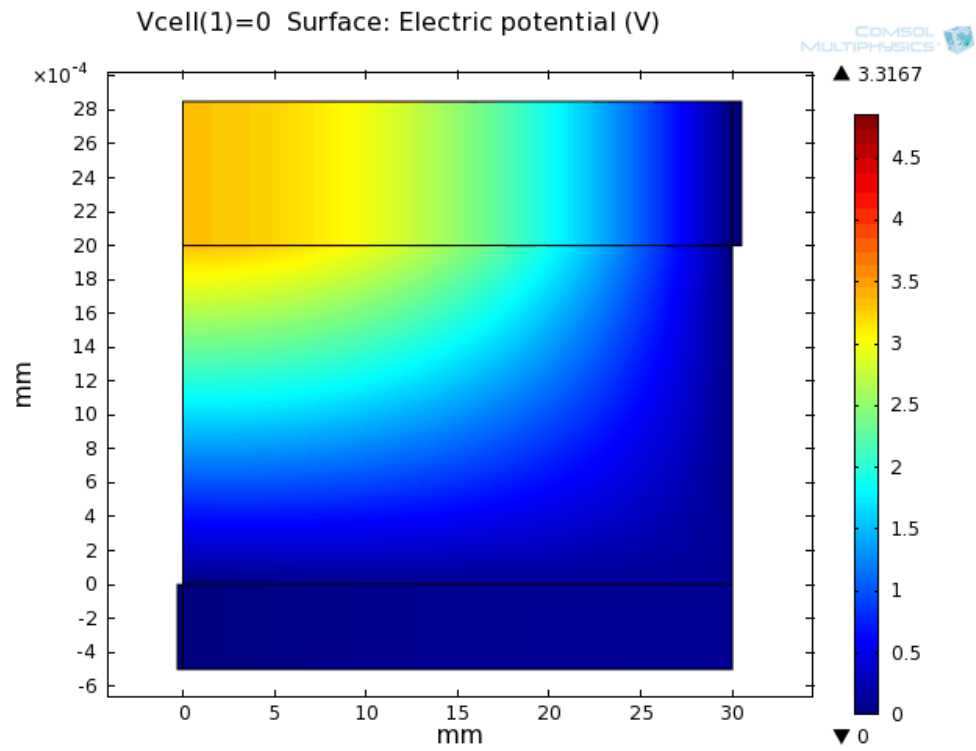


Figure 16. Potential distribution in the CIGS model with  $V_{\text{cell}}=0\text{V}$  (top) and  $V_{\text{cell}}=1.5\text{V}$  (bottom).

### 3.5 Model Validation

Model validation was conducted using a modified commercial CIGS module. The obtained commercial CIGS module was modified into a mini-module consisting of three cells (3x10 cm) connected in series. This mini-module was further tested with the Oriel QE/IPCE solar simulator (Appendix D). Prior to testing, manufacturer suggested exposing the module to sunlight for 3-4 days. However, due to cloudy weather condition, the module was exposed to the simulated ultraviolet (UV) light in UV light chamber for 2 days. This method may enhance the initial maximum sunlight absorption.

After testing, Scanning Electron Microscopy (SEM) samples were prepared from randomly selected locations on the mini-module. A total of 500 measurements for the thickness of the CIGS absorber layer were obtained through SEM, and Figure 17 shows the normal density function distribution fitting. The average and standard deviation of the absorber layer thickness were found to be 1.208  $\mu\text{m}$  and 0.305, respectively as shown in Table 6.

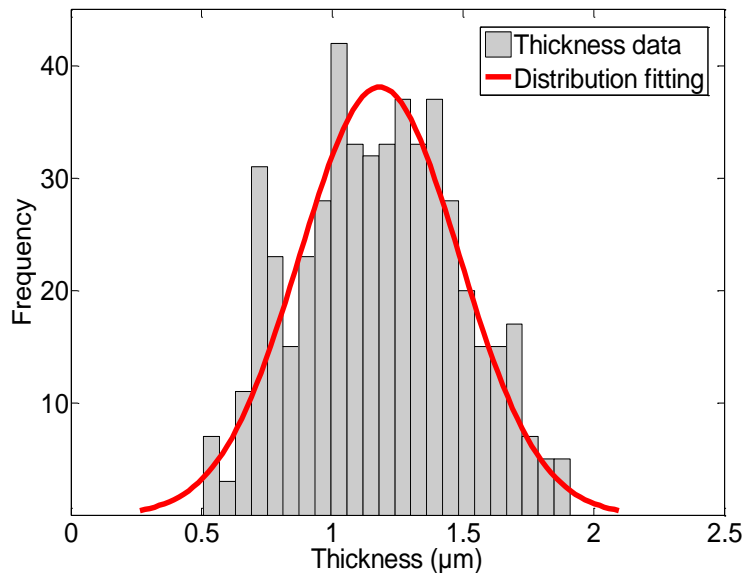


Figure 17. Histogram for thickness of CIGS absorber layer.

TABLE 6

STATISTICAL PROPERTIES OF ABSORBER LAYER THICKNESS

Properties	Value ( $\mu\text{m}$ )
<b>Mean</b>	<b>1.1805</b>
Standard Deviation	0.3054
Variance	0.0933
Kurtosis	2.3169
Skewness	0.0560

For validation purposes, the simulation model was tuned to fit the commercial CIGS module by using the average thickness of CIGS layer that was previously obtained by SEM. Moreover, there was no fluctuation of irradiance introduced in the developed model. The simulation was performed so as to mimic the conditions during testing, where there was only a constant inward light current density ( $J_{L,in}$ ). Figure 18 shows the comparison between the results obtained from direct measuring and simulation results. There is 1.8% error exists between the simulated and the measured results. The error is calculated from the delta power output between two curves over the total power output of both curves.

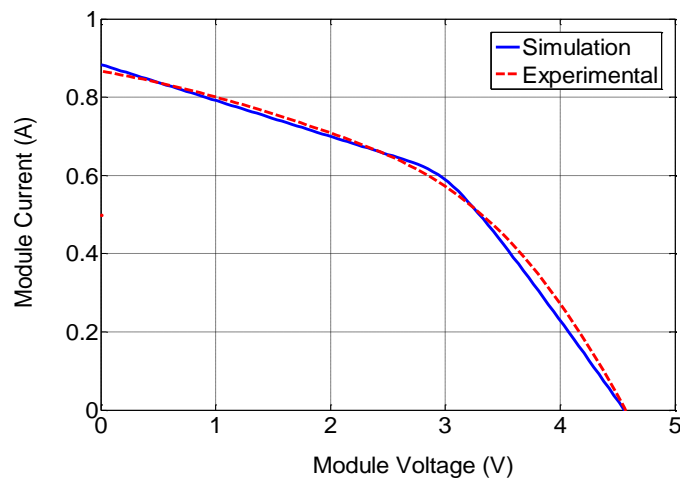


Figure 18. I-V Curve from direct measuring and simulation.

### 3.6 Case study

In order to better understand how the CIGS solar cell behaves, three case studies are performed in MATLAB. The CIGS input to MATLAB is the same as the one developed in COMSOL. Case studies 1 and 2 study the effect of CIGS structures (width and thickness of ZnO:Al), and Case study 3 studies the effect of the operating conditions on the output performance.

#### 3.6.1 Overview of the Case Studies

##### *Case Study 1: Cell Width*

In this case study, a CIGS module is developed with dimensions of 8.0cm x 10.0cm with series connection. The number of cells inside a module depends on the width of the cells. Module consists of cell with wider surface area means fewer cells in that particular module; and vice versa Width of the cells is varied from 3mm to 11mm. Other parameters, such as conductivity, resistance, transmittance, initial value for light generated currents and diode current are the same as listed in Table 5. The CIGS module is not subjected to any operating conditions (ie. no irradiance effect). The results of this case study are shown in Figure 19a and 19b.

##### *Case Study 2: ZnOAl Thickness*

Similar with the first case study, the CIGS module consists of 16 5mm-CIGS cells connected in series with no irradiance effect is used in the case study 2. In this case, the thickness of ZnO:Al ( $d_{ZnO:Al}$ ) is studied by varying the thickness from 0.5 $\mu$ m to 6.5 $\mu$ m, while keeping the same cell width (same number of cell in a module). Transmittance of ZnO:Al depends strongly on  $d_{ZnO:Al}$  as shown in the relationship between equation (2.1) and (2.2). The results are given in Figure 19c and 19d.

### *Case Study 3: Effect of Irradiance*

In order to mimic reality, operating conditions are introduced in this case study. This case study specifically studies the behavior of the output parameters (power output in a given day) when subject to the irradiance as described in Section 3.2.1. Similar module used in case study 2, the CIGS module consists of 16 series-connected cells with a width of 5mm is studied in this case study. Other parameters are unchanged and are listed in Table 5. The results of this case study are shown in Figure 19e and 19f.

### **3.6.2 Results and Discussion**

#### *Case Study 1: Cell Width*

The graphical results for case study 1 are shown in Figure 19a and 19b. The numerical results are tabulated in Table 7. As seen in Figure 19a, there exists a trade-off observed between current and voltage when the width of the cell is varied. As the cell width is increased, there are fewer series-connected cells in the module; this explains the voltage decrease with larger cell width. The voltage decrease is also due to how the cells are connected; the relationship between series and parallel connection has been previously discussed in Section 2.3.6.

Depending on the application, if higher current is desired, the design of the CIGS module should consist of cells with larger surface area. Looking at the power output in Figure 19b, although there is not much variation in the cells (Table 7), there is an optimum point observed for power output. The maximum power ( $P_{max}$ ) is observed in a 9mm cell for this particular case study scenario.

### *Case Study 2: ZnO:Al Thickness*

For the second case study, the thickness of the front contact has proven to have an effect on the performance output. This is seen in Figure 19c for net current output and Figure 19d for power output. Although the effect is not as apparent as compared to Case 1, maximum performance output ( $P_{max}$ ) is observed for the minimum thickness of ZnO:Al, which is equal to 0.5 $\mu$ m. This is because it is harder for light to penetrate a thicker front contact and thus, the thinner ZnO:Al layer is preferred. If the thickness is increased by 6.5 $\mu$ m, the power output drops by almost 15% (Table 8). Although the thinner front contact layer is preferred, the thickness must also be thick enough to absorb all the photons from the sunlight. Aside from the thickness issues, the front contact's transparency is also another factor that contributes to the amount of photons absorbed by the solar cell. This transparency also could have an effect in power generation.

### *Case Study 3: Effect of Irradiance*

The results for case study three is shown in Figure 19e for current and Figure 19f for power characteristics. The numerical results are tabulated in Table 9. The maximum current and power is observed at noon (time= 12pm) as the maximum irradiance ( $y_{max}= 1000\text{W}/\text{m}^2$ ) occurs at the same time. The current output highly depends on the irradiance as shown in the relationship of equation (2.4) and equation (2.13). Another conclusion that can be drawn from this case study is that, although the maximum power output (Figure 19f) is observed when the voltage is 6.0 V, this does not imply that the overall power generated in a day ( $P_{total}$ ) is the maximum at that same applied voltage. According to Table 9, the highest overall power output generated in a day is when the voltage is set to 7.0V.

TABLE 7

CASE STUDY 1:  $I_{sc}$  and  $P_{max}$  OUTPUT FOR DIFFERENT CELL WIDTH

<b>Width</b>	<b><math>I_{sc}</math> (A)</b>	<b><math>P_{max}</math> (W)</b>
3 mm	0.0893	1.2378
5 mm	0.1555	1.2812
7 mm	0.228	1.2952
9 mm	0.2878	1.2995
11mm	0.3539	1.2991

TABLE 8

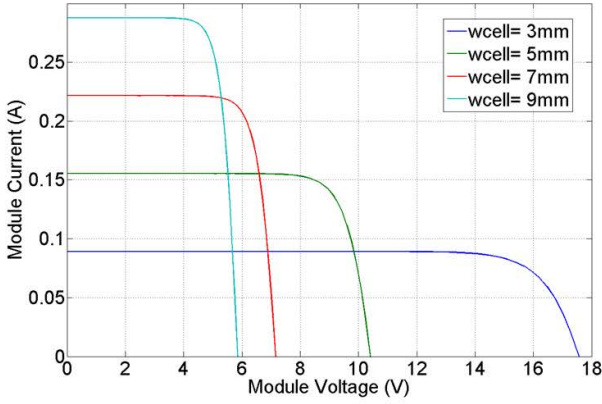
CASE STUDY 2:  $I_{sc}$  and  $P_{max}$  OUTPUT FOR DIFFERENT ZnO:Al THICKNESS

<b>d (<math>\mu\text{m}</math>)</b>	<b><math>I_{sc}</math> (A)</b>	<b><math>P_{max}</math> (W)</b>
0.5	0.1565	1.2897
2.5	0.1479	1.2159
4.5	0.1406	1.1540
6.5	0.1339	1.0971

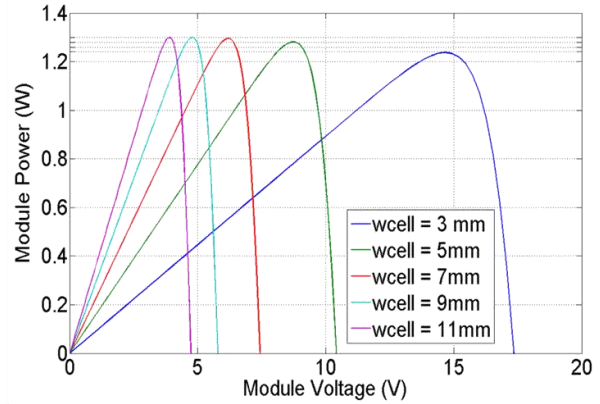
TABLE 9

CASE STUDY 3: OVERALL POWER OUTPUT IN A GIVEN DAY

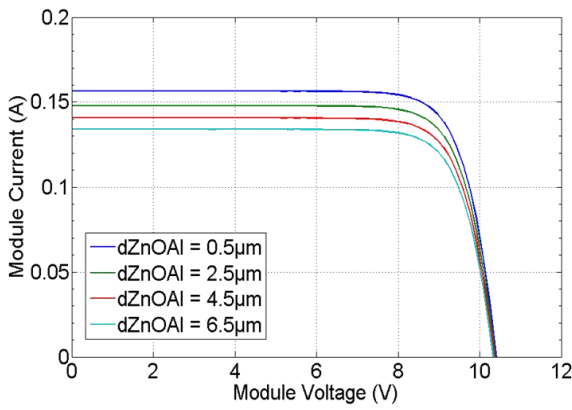
<b>V (V)</b>	<b><math>P_{total}</math> (W)</b>	<b>V (V)</b>	<b><math>P_{total}</math> (W)</b>
1	0.9160	5	4.5529
2	1.8320	6	5.3240
3	2.7476	7	5.6475
4	3.6606	8	5.0485



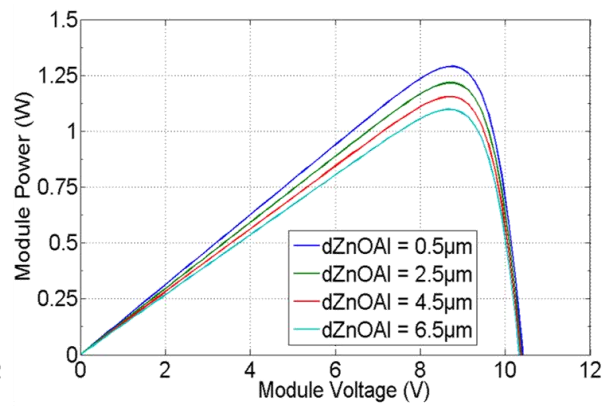
(a) Case 1: I-V Curve



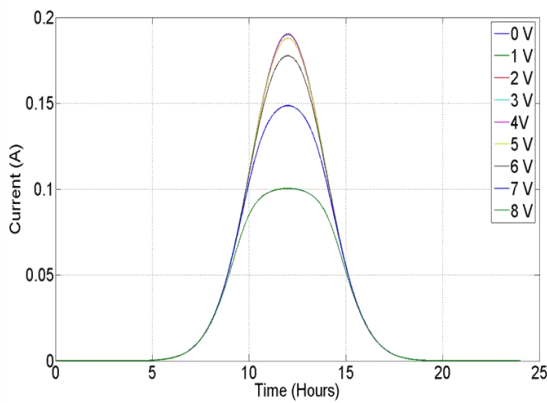
(b) Case 1: P-V Curve



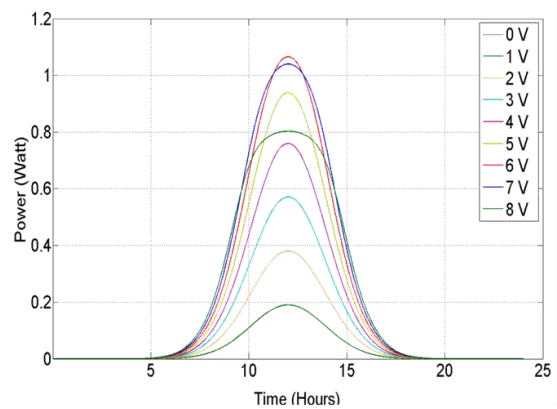
(c) Case 2: I-V Curve



(d) Case 2: P-V Curve



(e) Case 3: Current characteristics



(f) Case 3: Power characteristics

Figure 19. Output performance measured in current and power for Case 1 (a-b), Case 2 (c-d) and Case 3(e-f).

## CHAPTER 4

### DESIGN OPTIMIZATION OF SOLAR CELL MATERIAL STRUCTURE

#### 4.1 Reliability-Based Robust Design Optimization (RBRDO)

Uncertain operating conditions and manufacturing variability present on the thin-film solar cell system can be classified as aleatory and epistemic uncertainties. An aleatory uncertainty, which is presumed to be the inherent randomness of a phenomenon, can be treated as random variables [39-41]. On the other hand, epistemic uncertainty is classified by uncertainty that is caused by lack of knowledge or data, and can be treated by fuzzy variables [39-42]. The data sizes obtained to describe the uncertainties may be sufficient or insufficient, and this made it hard to consistently deal with such uncertainty data in predictive modeling and design [43].

To properly handle the uncertainty data for random inputs, the RBRDO approach is taken for modeling the thin film solar cells. RBRDO, which is heavily based on the distributions of design variables, could be implemented to optimize design under aleatory uncertainties [40, 41]. The physical structures of the cells are considered as random variables, and the input of the operating conditions, as mentioned in Section 2.3, are modeled based on a Gaussian distribution. Knowing that uncertainties exist in the thin film PV system, RBRDO can be formulated as [16, 43-50]:

$$\begin{aligned} & \text{minimize } C(\mathbf{X}; \mathbf{d}) \\ & \text{subject to} \\ & P_B(G_i(\mathbf{X}; \mathbf{d}) \leq 0) \geq \Phi(\beta_i), \quad i = 1, \dots, np \\ & \mathbf{d}^L \leq \mathbf{d} \leq \mathbf{d}^U, \quad \mathbf{d} \in R^{nd} \text{ and } \mathbf{X} \in R^n \end{aligned} \quad (4.1)$$

where  $P_B(G_i(\mathbf{X}; \mathbf{d}) \leq 0) = R_i(\mathbf{X}; \mathbf{d})$  is the system reliability, where  $G_i(\mathbf{X}; \mathbf{d}) \leq 0$  is defined as a safety event,  $C(\mathbf{X}; \mathbf{d})$  is the objective function or the cost function, and  $\mathbf{d} = \mu(\mathbf{X})$  is the design vector.  $\mathbf{X}$  is random vectors, respectively.  $\beta_i$  is a prescribed target reliability index. The numbers of

probabilistic constraints, design variables, and random variables, are noted as  $np$ ,  $nd$ , and  $n$ , respectively.  $\mathbf{d}^L$  and  $\mathbf{d}^U$  is lower and upper limit. Among all the random variables in a system, if the parameters describing a random variable are controllable, they are considered as design variables [43]. As an example, a random variable with a normal distribution may have two design variables, mean and standard deviation.

RBRDO is not a new approach. It is the combination of Random design (RD) and Reliability-based design optimization (RBDO). In mechanical design optimization, RBDO uses limited states function to separate the probability density function (PDF) of stress and strength to achieve higher reliability target [16]. RBDO accepts variability but does not attempt to minimize the variability that present in the system [16]. On the other hand, RD minimizes the quality loss of the product by reducing the effects of the source of variation without eliminating the source [16, 44]. The integration between RBDO and RD complement each other and thus called RBRDO. RBRDO approach is shown in Figure 20.

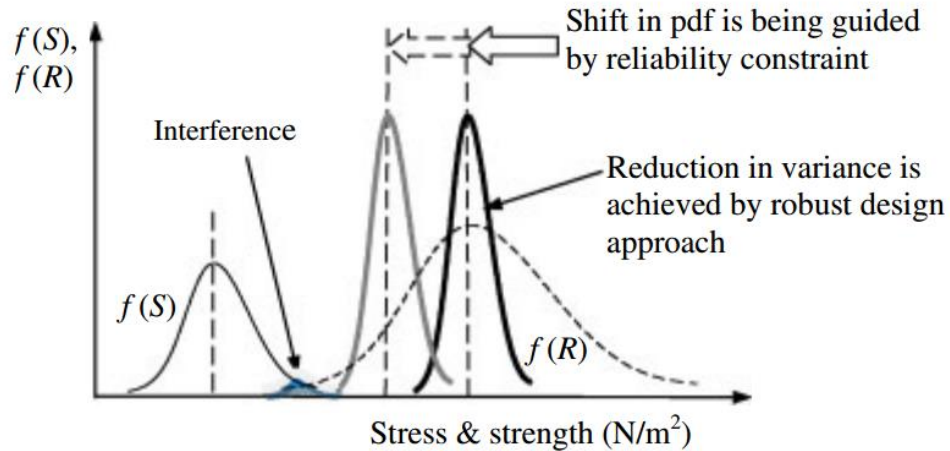


Figure 20. RBRDO approach [16].

## 4.2 Design Case Study

In this section, a thin-film solar cell design modeling problem is used to demonstrate the optimization method through the RBRDO approach. Thickness of the absorber layer in the thin film PV system is an important design parameter. As seen in Figure 4, a variation exists on the thickness of the absorber layer. Moreover, if the thickness of the CIGS absorber layer is minimized to an optimum thickness, the cost of the thin-film could be further reduced. This may yield a better cost-performance ratio than traditional silicon solar cells. However, depending on the surface area of the PV cell, the thickness of the absorber layer should be sufficient to absorb most of the photons from sunlight. In order to find the best combination of physical structures and to minimize variation while maintaining performance output, both physical parameters (width and thickness) are optimized in this section.

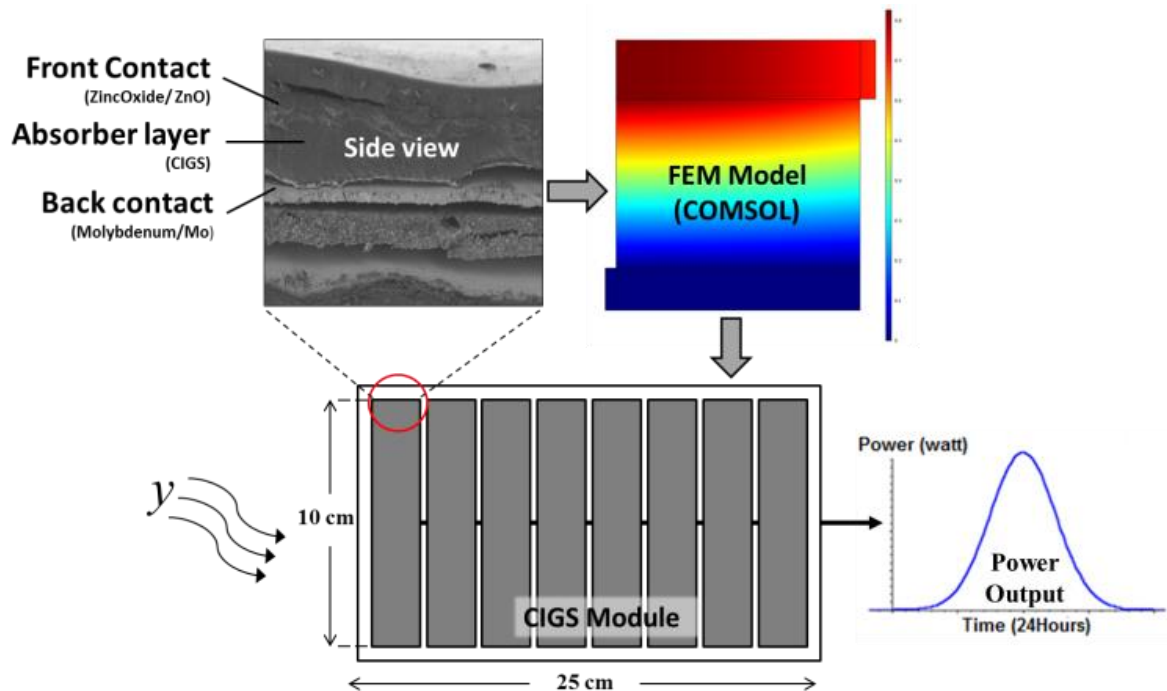


Figure 21. Studied multidimensional PV system.

Overview of the design case study is illustrated in Figure 21. As discussed in Section 2, a single CIGS Finite Element Method (FEM) model is developed in order to capture the I-V characteristics. Under operating condition that was described in Section 2.3, the performance output of the CIGS panel was characterized using properties obtained from the FEM model. Random properties (Table 10) were further introduced in the CIGS panel model. Finally, RBRDO was employed as the optimization approach for this particular case study.

#### 4.2.1 Description of the Design Problem

Three random variables are used in the design problem: two parameters of physical structures of the cells and one irradiance parameter. Their complete statistical properties are listed in Table 10.

TABLE 10  
RANDOM PROPERTIES FOR CIGS SOLAR CELL MODEL

Random Variable	$d_L$	$\mu_x=d$ (Mean)	$d_u$	Standard Deviation	Distribution Type
$X_1$ (cm)	1.0	3.0	10	0.3	Normal
$X_2$ ( $\mu\text{m}$ )	1.0	1.2	4.0	0.3	Normal
$X_3$ (irradiance)	NA	0.5	NA	0.1	Normal

The physical structure of thin-film solar cell, width of the cell ( $X_1$ ), and thickness of the absorber layer ( $X_2$ ) are considered as aleatory uncertainties. Both random variables are considered as design variables  $d = [d_1, d_2]^T$ , and both are normally distributed:  $X_1 \sim N(\mu_1, 0.3)$  and  $X_2 \sim N(\mu_2, 0.3)$ . The initial values for  $X_2$  are obtained from SEM observation as mention in section 2.4. Epistemic uncertainties, irradiance ( $X_3$ ) is not considered as a design variable. To take account for uncertainties during operating condition, maximum irradiance for one ideal-day is modeled as randomly generated samples assuming  $X_3 \sim N(0.5, 0.1)$ . In this study, the reliability is

set to be  $\Phi(\beta_{t_i}) = 90\%$  and series resistance ( $R_s$ ) is considered as the constraint. The design problem is formulated as follows:

$$\begin{aligned}
 & \text{minimize} && \text{Var}\{\text{Power}(d_1, d_2)\} - \text{Mean}\{\text{Power}(d_1, d_2)\} \\
 & \text{subject to} && P_B(R_s \leq 25) \geq \Phi(\beta_{t_i}) \\
 & && 1.0 \leq d_1 \leq 10.0 \\
 & && 0.5 \leq d_2 \leq 4.0
 \end{aligned} \tag{4.2}$$

#### 4.2.2 Design Case Study Results

The design optimization of the solar cell material structure is converged to the optimum design after 19 iterations. The iterative design history during the optimization process is tabulated in Table 11. Figure 22 illustrates the probability density functions (PDF) of the initial and the optimum designs. The mean power output is improved through the RBRDO while minimizing the standard deviation in the system. Comparing the optimum design obtained with the initial design (Figure 23), the objective function has been substantially reduced. Specifically, the variance is reduced from 2.9203 to 1.7943 (~33.4%), while the mean value of the power output is increased from 8.2426 W to 8.5574 W (~3.7%).

The improvement of 3.7% of mean power output does not seem to be superior because the RBRDO approach depends heavily on the specified initial conditions. Since the initial conditions for the case study are obtained from commercial CIGS solar cells which had passed their manufacturer's quality control tests, the properties of the initial design (before application of the RBRDO approach) may be said to be good in and of itself. This explains why there is not much of an improvement observed in the mean power output. It may be further concluded that both width and thickness of the absorber layer are interacting with each other. The right combination of the cell's physical structure is essential in enhancing output performance. In real life, the impact of reduction in variance of the power output also reduces the number of solar

panel required to generate a certain output. For example, in order to produce 20kW of energy in a day, a system composed of n-number of panels should be able to produce at least 4kW per hour at 5 hours of direct sunlight. To account for variability in power production of the solar panel, the system typically requires additional panels in order to be able to continuously supply the demand of 20kW daily. With solar panels that have less variability, the requirement for these additional panels will also be minimized. The impact of this may be greater for PV power stations (as compared to residential applications), since they are large-scale operations.

RBRDO is a general optimization methodology and its implementation is not limited to thin films cell, It can be integrated with any types of solar cells. RBRDO can be used as an assessment tool for new PV technologies because it provides for optimal design solutions. RBRDo also assists in attaining robust performance, efficiency, and stability

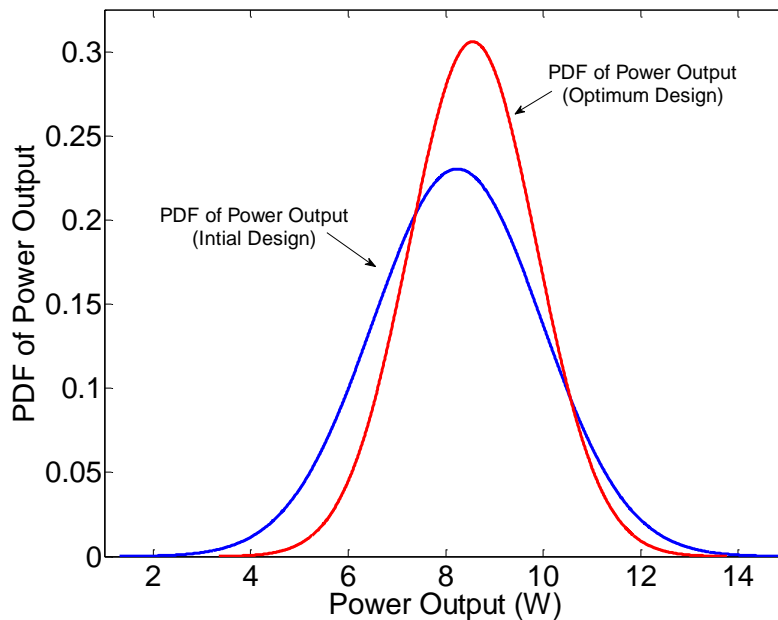
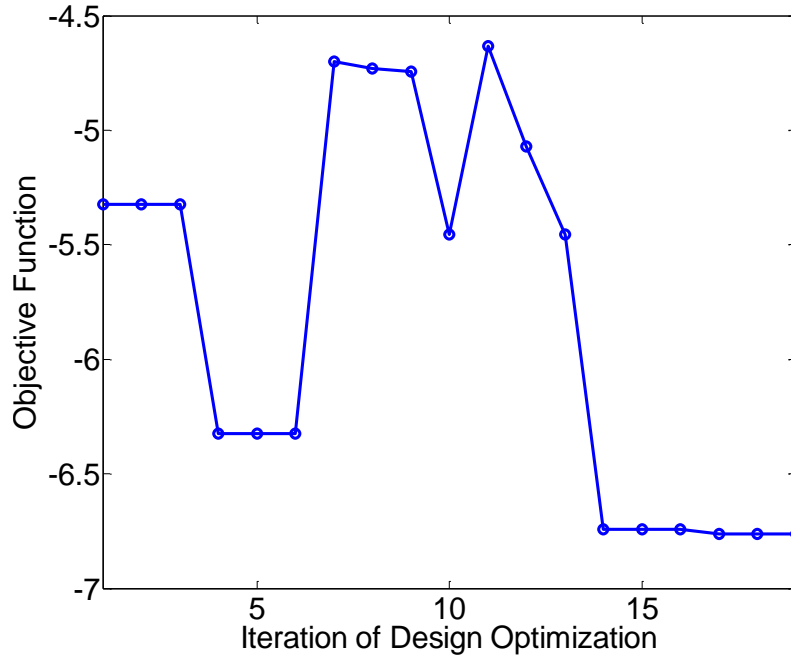


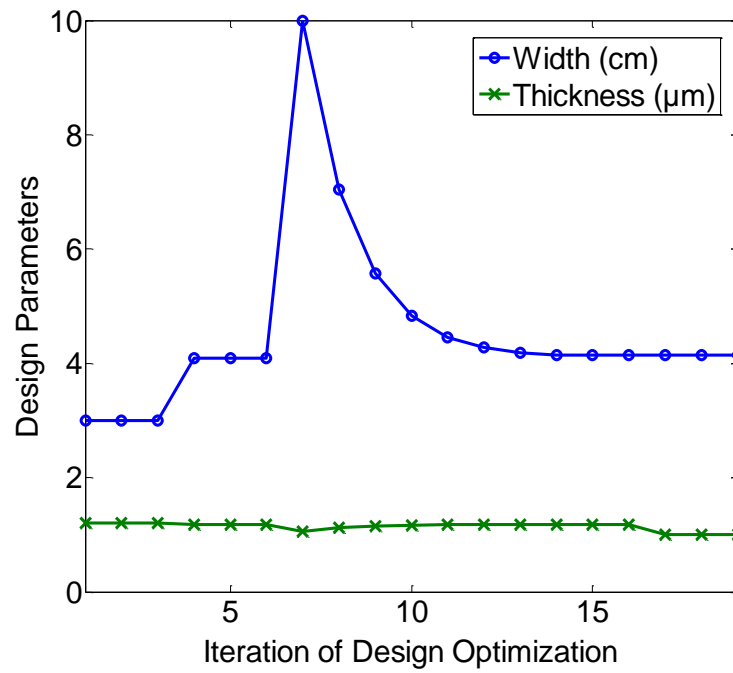
Figure 22. PDF of the mean power output at initial and optimum design.

TABLE 11  
ITERATION HISTORY OF RBRDO

Iteration	Design variables		Variance Power Output (Watt)	Mean Power Output (Watt)	Objective Function
	X <sub>1</sub> (cm)	X <sub>2</sub> (μm)			
<b>Initial</b>	3.0	1.2	2.9203	8.2426	<b>-5.3223</b>
2	3.0	1.2	2.9203	8.2426	-5.3223
3	3.0	1.2	2.9203	8.2426	-5.3223
4	4.0915	1.1840	2.1069	8.4323	-6.3254
5	4.0915	1.1840	2.1069	8.4323	-6.3254
6	4.0915	1.1840	2.1069	8.4323	-6.3254
7	10.00	1.0550	2.1851	6.8846	-4.6995
8	7.0458	1.1195	2.5353	7.2677	-4.7324
9	5.5686	1.1517	2.9120	7.6547	-4.7427
10	4.8301	1.1678	2.8417	8.2972	-5.4555
11	4.4608	1.1759	3.0275	7.6620	-4.6345
12	4.2762	1.1799	2.2732	7.3444	-5.0712
13	4.1838	1.1819	1.7298	7.1857	-5.4559
14	4.1377	1.1830	1.7856	8.5275	-6.7419
15	4.1383	1.183	1.7856	8.5275	-6.7419
16	4.1383	1.183	1.7856	8.5275	-6.7419
17	4.1377	1.0	1.7943	8.5574	-6.7631
18	4.1377	1.0	1.7943	8.5574	-6.7631
<b>Optimum</b>	4.1377	1.0	1.7943	8.5574	<b>-6.7631</b>



(a) Cost function



(b) Design variables

Figure 23. RBRDO design history.

## CHAPTER 5

### CONCLUSIONS AND FUTURE WORK

#### 5.1 Conclusions

A functional thin film solar cell model has been developed. This model takes account the manufacturing variability, material properties and operating condition. Dealing with uncertainties data for random inputs are inevitable in modeling thin film solar cells or any PV system in general. These random inputs include the geometry structure (width and thickness of absorber layer), and also the uncertain level of irradiance. This paper proposed a reliability-based robust design optimization approach in order to yield a more robust performance output of the thin film solar cell, while minimizing the presence of variability and uncertainties in the design system. The case study presented elaborate upon the functionality of the proposed approach, with only aleatory random variables are considered as design input. The results of the case study show that the proposed approach was able to find the optimum combination between the design parameters, width of the cell, and thickness of the absorber layer. Comparing to the initial design, the optimum design turns out to be more robust in terms on power output generation.

#### 5.2 Future Work

For future work, more constraints, such as the level of transmission through the front contact layer and percentage of material in the system, will be implemented. A larger-scale solar cell model will also be employed in order to illustrate a more significant improvement. Moreover, in order to address the non-uniform thickness during modeling, a Ranfom Field approach will be implemented for this particular issue. Cloudy weather conditions will be implemented to mimic reality. Trade-off between material cost and power output is also another subject of interest for future work.

## REFERENCES

## REFERENCES

1. Edoff, M., *Thin Film Solar Cells: Research in an Industrial Perspective*. Ambio, 2012. 41: p. 112-118.
2. Oi, A., *Design and Simulation of Photovoltaic Water Pumping System*, in *Electrical Engineering*, 2005, California Polytechnic State University, San Luis Obispo, CA, USA. p. 113.
3. Johansson, J., *Modelling and Optimization of CIGS Solar Cell Modules*, in *Department of Architecture and Built Environment*, 2008, Lund University: Lund, Scania, Sweden.
4. IRENA, *Renewable Energy Technologies: Cost Analysis Series*, 2012.
5. Green, M.A., *The Future of Thin Film Solar Cells*. Proceedings of ISES Solar World Congress 2007: Solar Energy and Human Settlement, Vols I-V, 2007: p. 96-101.
6. Razykov, T.M., et al., *Solar Photovoltaic Electricity: Current Status and Future Prospects*. Solar Energy, 2011. 85(8): p. 1580-1608.
7. REN21, *Renwable 2012 Global Status Report*, 2012.
8. Nelson, J., *The Physics of Solar Cells*. 1<sup>st</sup> ed, 2003, London, UK: Imperial College Press.
9. Green, M.A., et al., *Solar Cell Efficiency Tables (version 40)*. Progress in Photovoltaics, 2012. 20(5): p. 606-614.
10. Repins, I., et al., *19.9%-Efficient ZnO/CdS/CuInGaSe<sub>2</sub> Solar Cell with 81.2% Fill Factor*. Progress in Photovoltaics, 2008. 16(3): p. 235-239.
11. Nakada, T., *Invited Paper: CIGS-based Thin Film Solar Cells and Modules: Unique Material Properties*. Electronic Materials Letters, 2012. 8(2): p. 179-185.
12. Singh, U.P. and S.P. Patra, *Review Article: Progress in Polycrystalline Thin-Film Cu(In,Ga)Se<sub>2</sub> Solar Cells*. International Journal of Photoenergy, 2010.
13. Dimmler, B. and H.W. Schock, *Scaling-up of CIS Technology for Thin-Film Solar Modules*. Progress in Photovoltaics, 1996. 4(6): p. 425-433.
14. Powalla, M. and B. Dimmler, *Scaling Up Issues of CIGS Solar Cells*. Thin Solid Films, 2000. 361: p. 540-546.
15. Karpov, V.G., A.D. Compaan, and D. Shvydka, *Micrononuniformity Effects in Thin-Film Photovoltaics*. Conference Record of the 29<sup>th</sup> IEEE Photovoltaic Specialists Conference, 2002: p. 708-711.

16. Yadav, O.P., S.S. Bhamare, and A. Rathore, *Reliability-based Robust Design Optimization: A Multi-objective Framework Using Hybrid Quality Loss Function*. Quality and Reliability Engineering International, 2010. 26(1): p. 27-41.
17. Rathod, V., et al., *Reliability-based Robust Design Optimization: A Comparative Study*, in 2011 IEEE International Conference on Industrial Engineering and Engineering Management (IEEM)2011: Singapore.
18. *Thin Film Solar Cells Fabrication, Characterization and Applications*. 1<sup>st</sup> ed, S.K. Peter Capper, Arthur Willoughby, 2006, Wiltshire, England: John Wiley & Sons, Ltd.
19. Schroeder, D.J., et al., *Hole Transport and Doping States in Epitaxial CuIn(1-x)Ga(x)Se(2)*. Journal of Applied Physics, 1998. 83(3): p. 1519-1526.
20. Coyle, J.D., *Life prediction for CIGS Solar Modules Part1: Modeling Moisture Ingress and Degradation*. Progress in Photovoltaics: Research and Applications, 2011.
21. Zunger, A., *Why does Ga Addition to CIS Limit its Cell Performance: The Amazing Physics of Grain-boundaries and Killer-defects in Chalcopyrites*, in DOE Solar Energy technologies, 2005: Denver, Colorado.
22. Coyle, D.J., et al., *Degradation Kinetics of CIGS Solar Cells*, in 34<sup>th</sup> IEEE Photovoltaic Specialists Conference, Vols 1-3, 2009: p. 2165-2169.
23. Malm, U. and M. Edoff, *Simulating Material Inhomogeneities and Defects in CIGS Thin-film Solar Cells*. Progress in Photovoltaics, 2009. 17(5): p. 306-314.
24. Burgelman, M. and A. Niemegeers, *Calculation of CIS and CdTe Module Efficiencies*. Solar Energy Materials and Solar Cells, 1998. 51(2): p. 129-143.
25. Kessler, J., et al., *Interface Engineering between CuInSe<sub>2</sub> and ZnO*. Conference Record of the 23<sup>rd</sup> IEEE Photovoltaic Specialists Conference, 1993: p. 447-452.
26. Amin, N., et al., *Numerical Modelling of Ultra Thin Cu(In,Ga)Se-2 Solar Cells*. International Conference on Materials for Advanced Technologies, Symposium O, 2012. 15: p. 291-298.
27. Tsai, H.L., *Insolation-Oriented Model of Photovoltaic Module using MATLAB/Simulink*. Solar Energy, 2010. 84(7): p. 1318-1326.
28. Gonzalez-Longatt, F.M., *Model of Photovoltaic Module in MATLAB*, in 2do Congreso Iberoamericano de Estudiantes de Ingeniería Eléctrica, Electrónica y Computación (II CIBELEC ), 2005: Puerto la Cruz, Venezuela.

29. Tsai, H.L., C.S. Tu, and Y.J. Su, *Development of Generalized Photovoltaic Model Using MATLAB/SIMULINK*. WCECS: World Congress on Engineering and Computer Science, 2008: p. 846-851.
30. Ramos Hernanz, J.A., et al., *Modelling of Photovoltaic Module*, in International Conference on Renewable Energies and Power Quality, 2010: Granada, Spain.
31. Kou, Q., S.A. Klein, and W.A. Beckman, *A Method for Estimating the Long-Term Performance of Direct-coupled PV Pumping Systems*. Solar Energy, 1998. 64(1-3): p. 33-40.
32. Skoplaki, E. and J.A. Palyvos, *On the Temperature Dependence of Photovoltaic Module Electrical Performance: A Review of Efficiency/Power Correlations*. Solar Energy, 2009. 83(5): p. 614-624.
33. Tiwari, G.N., *Solar Energy: Fundamentals, Design, Modelling and Applications*. 4<sup>th</sup> ed, 2009, Oxford, UK: Alpha Science International Ltd.
34. Villalva, M.G., J.R. Gazoli, and E. Ruppert, *Comprehensive Approach to Modeling and Simulation of Photovoltaic Arrays*. IEEE Transactions on Power Electronics, 2009. 24(5-6): p. 1198-1208.
35. Enrique, J.M., et al., *Theoretical Assessment of the Maximum Power Point Tracking Efficiency of Photovoltaic Facilities with Different Converter Topologies*. Solar Energy, 2007. 81(1): p. 31-38.
36. Adamo, F., et al., *Characterization and Testing of a Tool for Photovoltaic Panel Modeling*. IEEE Transactions on Instrumentation and Measurement, 2011. 60(5): p. 1613-1622.
37. Walker, G., *Evaluating MPPT Converter Topologies using a MATLAB PV Model*. Journal of Electrical & Electronics Engineering, Australia, 2001. 21(1): p. 49-55.
38. Solmetric, *Application Note PV A-600-1: Guide to Interpreting I-V Curve Measurements of PV Arrays*, 2011.
39. Kiureghian, A.D. and O. Didevsen, *Aleatory or Epistemic? Does It Matter?* Structural Safety, 2009. 31(2): p. 105-112.
40. Wei, J., B. Yang, and W. Liu, *Design Optimization Under Aleatory and Epistemic Uncertainties*. 8<sup>th</sup> IEEE International Conference on Dependable, Autonomic and Secure Computing, Proceedings, 2009: p. 491-495.
41. Huang, H.Z. and X.D. Zhang, *Design Optimization with Discrete and Continuous Variables of Aleatory and Epistemic Uncertainties*. Journal of Mechanical Design, 2009. 131(3).

42. Billinton, R. and D. Huang, *Aleatory and Epistemic Uncertainty Considerations in Power System Reliability Evaluation*, in 10<sup>th</sup> International Conference on Probabilistic Methods Applied to Power Systems, 2008: p. 302-309.
43. Wang, P.F., B.D. Youn, and L.J. Wells, *Bayesian Reliability Based Design Optimization using Eigenvector Dimension Reduction (EDR) Method*. Proceedings of the ASME International Design Engineering Technical Conferences and Computers and Information in Engineering Conference, 2007, Vol 6, Pts A and B, 2008: p. 1247-1262.
44. Youn, B.D., K.K. Choi, and K.Y. Yi, *Performance Moment Integration (PMI) Method for Quality Assessment in Reliability-based Robust Design Optimization*. Mechanics Based Design of Structures and Machines, 2005. 33(2): p. 185-213.
45. Du, X.P. and W. Chen, *Sequential Optimization and Reliability Assessment Method for Efficient Probabilistic Design*. Journal of Mechanical Design, 2004. 126(2): p. 225-233.
46. Tang, Y.F., J.Q. Chen, and J.H. Wei, *A Sequential Algorithm for Reliability-Based Robust Design Optimization Under Epistemic Uncertainty*. Journal of Mechanical Design, 2012. 134(1).
47. Wang, L., and Kodiyalam, S., *An Efficient Method for Probabilistic and Robust Design with Non-normal Distribution*, in 43<sup>rd</sup> AIAA SDM Conference. April 2002: Denver, Colorado.
48. Chen, X., Hesselman, T.K., and Neill, D. J., *Reliability-based Structural Design Optimization for Practical Applications*, in 38<sup>th</sup> AIAA SDM Conference. 1997.
49. Wu, Y.T., et al., *Safety-Factor based Approach for Probability-Based Design Optimization*, in 42<sup>nd</sup> AIAA/AASME/ASC/AHS/ASC SDM Conference & Exhibit. April 2001: Seattle, Washington.
50. Youn, B.D., Choi, K.K., and Du, L., *Enriched Performance Measure Approach (PMA+) for Reliability based Design Optimization*. AIAA Journal, 2005. 43(4): p. 874-884.

## APPENDICES

## APPENDIX A

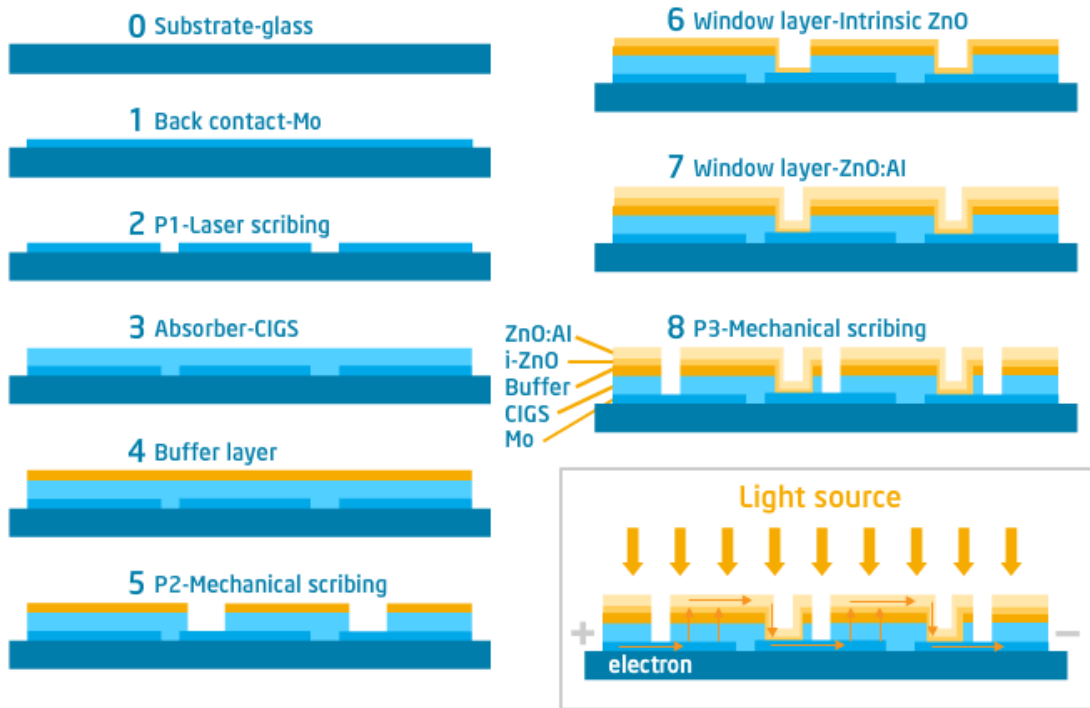
### AN OVERVIEW COMPARISON OF MAJOR PV TECHNOLOGIES (IRENA, 2012)

		1 <sup>st</sup> Generation PV		2 <sup>nd</sup> Generation PV			3 <sup>rd</sup> Generation PV		
Technology	Units	Single crystalline silicon (sc-Si)	Polycrystalline silicon (pc-Si)	Amorphous silicon (a-Si)	Copper Indium Gallium Diselenide (CIS/CIGS)	Cadmium Telluride solar cells (CdTe)	III-V compound Multijunction, Concentrated PV (CPV)	Dye-sensitized (DSSC)	Organic or Polymer (OPV)
Best research solar cell efficiency at AM1.5*	%	24.7		10.4 Single junction 13.2 Tandem	20.3	16.5	43.5	11.1	11.1
Confirmed solar cell efficiency at AM1.5	%	20-24	14-18	6-8	10-12	8-10	36-41	8.8	8.3
Commercial PV Module efficiency at AM1.5	%	15-19	13-15	5-8	7-11	8-11	25-30	1-5	1
Confirmed maximum PV Module efficiency	%	23	16	7.1 / 10.0	12.1	11.2	25	-	-
Current PV module cost	USD/W	< 1.4	< 1.4	~ 0.8	~ 0.9	~ 0.9	-	-	-
Market share in 2009	%	83	3	1	13		-	-	-
Market share in 2010	%	87	2	2	9		-	-	-
Maximum PV module output power	W		320	300	120	120	120	-	-
PV module size	m <sup>2</sup>	2.0	1.4-2.5	1.4	0.6-1.0	0.72	-	-	-
Area needed per kW	m <sup>2</sup>	7	8	15	10	11	-	-	-
State of commercialisation		Mature with large-scale production	Mature with large-scale production	Early deployment phase, medium-scale production	Early deployment phase, medium-scale production	Early deployment phase, small-scale production	Just commercialised, small-scale production	R&D phase	R&D phase

*\*Note: Standard Testing Conditions, temperature 25°C, light intensity 1000W/m<sup>2</sup>, air mass 1.5.*

## APPENDIX B

### PROCESS FLOW OF MONOLITHIC INTERCONNECTION CIGS MODULE

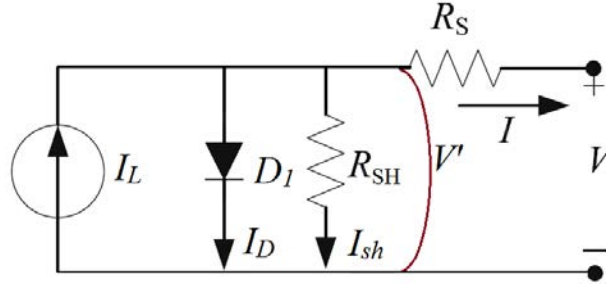


Reference: AU Optronics Corp. (<http://auo.com>)

## APPENDIX C

### KIRCHHOFF'S LAW AND OHM'S LAW

One-Diode Model:



Kirchhoff's Law:

$$\sum_{k=1}^n I_k = 0$$

where  $I_k$  is current in branch  $k$ ,  $n$  is the number of branches in a node. The net current output ( $I$ ) shown in the one-diode model, can be represented as:

$$I = I_L - I_D - I_{sh}$$

where  $I_L$  is light generated current,  $I_D$  is diode current and  $I_{sh}$  is current due to shunt resistance.

Ohm's Law:

$$R = \frac{V}{I}$$

where  $R$  is resistance,  $V$  is voltage and  $I$  is current. The net output voltage ( $V$ ) shown in the one-diode model, can be represented as the total of shunt voltage ( $V'$ ) and series voltage ( $V_s$ ):

$$V = V' + V_s$$

$$V = V' + I \cdot R_s$$

Thus, the diode equation given in equation (2.7) can be rewrite as:

$$I_D = I_o \left[ e^{\left(\frac{qV}{AkT_c}\right)} - 1 \right] = I_o \left[ e^{\left(\frac{q(V' + I \cdot R_s)}{AkT_c}\right)} - 1 \right]$$

APPENDIX D

EXPERIMENT SET UP

